

# The High Resolution *IRAS* Galaxy Atlas

Yu Cao

Division of Physics, Mathematics, and Astronomy, California Institute of Technology,  
Pasadena, California 91125

Susan Terebey

Extrasolar Research Corporation, Pasadena, California 91106

Thomas A. Prince

Division of Physics, Mathematics, and Astronomy, California Institute of Technology,  
Pasadena, California 91125

Charles A. Beichman

Infrared Processing and Analysis Center, California Institute of Technology,  
Pasadena, California 91125

## ABSTRACT

An atlas of the Galactic plane ( $-4.7^\circ < b < 4.7^\circ$ ) plus the molecular clouds in Orion,  $\rho$  Ophiuchus, and Taurus-Auriga has been produced at 60 and 100  $\mu\text{m}$  from *IRAS* data. The atlas consists of resolution-enhanced coadded images having  $1' - 2'$  resolution as well as coadded images at the native *IRAS* resolution. The *IRAS* Galaxy Atlas, together with the DRAO HI line / 21 cm continuum and FCRAO CO (1-0) line Galactic plane surveys, both with similar ( $\sim 1'$ ) resolution, provide a powerful venue for studying the interstellar medium, star formation and large scale structure in our Galaxy. This paper documents the production and characteristics of the Atlas.

*Subject headings:* astronomical data bases: atlases — Galaxy: structure — HII regions — infrared: ISM: continuum — stars: formation — techniques: image processing

## 1. Introduction

In 1983 the *Infrared Astronomical Satellite* fundamentally changed our view of the infrared sky when it conducted the first infrared all sky survey. The *IRAS* data have

proven important to the study of many astrophysical phenomena including star formation, the interstellar medium, Galactic structure, late-type stars, supernova remnants, external galaxies, infrared cirrus, and debris disks around nearby stars (Beichman 1987). Newer infrared spacecraft missions such as ISO, MSX, and IRTS now provide higher sensitivity and spatial resolution (Kessler 1995, Matsumoto 1995, Price 1995, Mill & Guilmain 1996). However, by design they cover only a small fraction of the sky, thus ensuring the *IRAS* data will provide a fundamental archive for many years to come.

The native spatial resolution of the *IRAS* coadded data is a few by five arcminutes. Various image reconstruction techniques have been applied to the *IRAS* data in the quest to extract higher spatial resolution (Terebey & Mazzarella 1994). These include maximum entropy techniques, among them the HIRAS package developed at Groningen (Assendorp et al. 1995, Bontekoe et al. 1994). Making use of an alternate approach, the production of the *IRAS* Galaxy Atlas is based on the well-known HIRRES processor, first developed in 1991 and made available to the scientific community by the Infrared Processing and Analysis Center (IPAC). HIRRES implements the iterative Maximum Correlation Method (MCM; Aumann, Fowler, & Melnyk 1990), a variant of the Richardson-Lucy algorithm which has been optimized for *IRAS* data. The advantages of HIRRES include flux conservation, speed of processing, and the ability to work reliably on faint sources. HIRRES images have been successfully used for a variety of Galactic and extragalactic studies (Rice 1993, Surace et al. 1993, Terebey & Mazzarella 1994).

The parallel supercomputing facilities available at Caltech and the development of new artifact reduction algorithms made possible a large-scale high-resolution *IRAS* mapping of the Galactic plane (Cao et al. 1996, hereafter referred to as Paper I, Cao 1997). The new *IRAS* Galaxy Atlas (IGA) maps have  $1' - 2'$  resolution. This represents a three-fold improvement in linear resolution for a total factor of ten improvement in areal resolution over the *IRAS* Sky Survey Atlas (ISSA; Wheelock et al. 1994). The IGA incorporates several important differences from standard HIRRES processing at IPAC. Foremost is improved destriping and zodiacal emission subtraction, which lead to reduction of artifacts, enhancement of faint structure, and the ability to mosaic images without edge discontinuities. The IGA is well suited to high-resolution studies of extended structure, and will be valuable for a wide range of scientific studies, including: the structure and dynamics of the interstellar medium (ISM); cloud core surveys within giant molecular clouds; detailed studies of HII regions and star forming regions; determination of initial mass functions (IMFs) of massive stars; and study of supernova remnants (SNRs). The IGA will be especially useful for multi-wavelength studies using the many Galactic plane surveys that have similar ( $\sim 1'$ ) resolution. These include the new FCRAO CO(1-0) spectral line (Heyer 1996) and DRAO HI line / 21 cm continuum surveys (Normandeau, Taylor, & Dewdney

1997).

All image reconstruction algorithms have their quirks. This paper describes and characterizes the IGA so that it will be useful for quantitative scientific study. Section 2 describes the geometry and information content of the atlas images. Section 3 gives a description on the various processing stages, namely the basic algorithm, subtraction of zodiacal emission, and coordinate transform and reprojection. Section 4 discusses the characteristics of the images, including resolution, photometric and positional accuracy, mosaic properties, and calibration. Section 5 details the various image artifacts.

The IGA images are available upon request from IPAC ([info@ipac.caltech.edu](mailto:info@ipac.caltech.edu); <http://www.ipac.caltech.edu>) or through the NASA National Space Science Data Center (NSSDC; [http://nssdc.gsfc.nasa.gov/nssdc/nssdc\\_home.html](http://nssdc.gsfc.nasa.gov/nssdc/nssdc_home.html)). The complete archive is comprised of ten 8mm tapes. Casual users should direct requests for specific images to IPAC. This paper gives references to online resources (mostly in the form of World Wide Web documents) whenever appropriate. The information is accurate as of 1997.

## 2. Description of the Atlas

The atlas consists of images (1st and 20th iteration) and ancillary maps in FITS (Wells, Greisen, & Harten 1981) format in the 60 and 100  $\mu\text{m}$  wavelength bands. The Galactic plane images cover  $0^\circ \leq l < 360^\circ$  in Galactic longitude and  $-4.7^\circ < b < 4.7^\circ$  in latitude. The field of view for each image is  $1.4^\circ \times 1.4^\circ$ , on  $1^\circ$  centers in both the Galactic longitude and latitude directions, the pixel size is  $15''$ , and Galactic coordinates and Cartesian projection are used. The molecular cloud fields (Orion,  $\rho$  Ophiuchus, Taurus-Auriga) are rectangular, about  $20^\circ$  on a side, with boundaries selected to encompass the diffuse infrared emission of each cloud. The images are  $2.5^\circ \times 2.5^\circ$  on  $2^\circ$  centers with  $15''$  pixels and use Equatorial coordinates (B1950) and Cartesian projection. The boundaries are given by: Orion [ $5^h 8^m, 6^h 12^m$ ] [ $-13^\circ 0, 18^\circ 0$ ],  $\rho$  Ophiuchus [ $15^h 31^m, 17^h 00^m$ ], [ $-33^\circ 0, -17^\circ 0$ ], and Taurus-Auriga [ $3^h 48^m, 5^h 12^m$ ], [ $12^\circ 0, 33^\circ 0$ ]. References to IGA sources in the Galactic plane should follow the sample format IGA G218.50 – 0.50, while the names of sources in molecular clouds should follow the *IRAS* format, e.g. IGA B04302+2538 to represent the position ( $4^h 30^m 2, 25^\circ 38'$ , B1950). The Cartesian projection used with Equatorial coordinates is a relatively new FITS combination which may cause trouble for some FITS reading software. For individual images or small mosaicked fields the FITS header keyword `-SIN` can be used in place of `-CAR` (see Sec. 3.4).

The 1st iteration images are coadded *IRAS* images (i.e. FRESCO images) with no

resolution enhancement. They have the native *IRAS* resolution of approximately  $2.0' \times 4.7'$  at  $60 \mu\text{m}$  and  $3.8' \times 5.4'$  at  $100 \mu\text{m}$ . After MCM processing to 20 iterations the typical spatial resolution improves to  $1.0' \times 1.7'$  at  $60 \mu\text{m}$  and  $1.7' \times 2.2'$  at  $100 \mu\text{m}$  (see Sec. 4.1). The images at 60 and  $100 \mu\text{m}$  have inherently different resolutions. Ratio or color maps should only be attempted by expert users, and only after correcting the images to a common resolution.

Aperture photometry is accurate to about 25% (see Sec. 4.4). Most of the uncertainty is due to background measurement uncertainties. The images are on the same absolute flux level as the ISSA images, except for a constant AC/DC factor (see Sec. 4.3).

The ancillary maps include the correction factor variance (CFV) map, the photometric noise (PHN) map, coverage (CVG) map, the detector track (DET) map, and the beam sample map (BEM). See Table 1 in Section 3.2 for the quantities they represent and Section 6 for example images. The FWHM.txt text file gives Gaussian beam sizes derived from the corresponding BEM map.

### 3. Description of Processing

For an overview of the HIRES processing developed at IPAC, see [http://www.ipac.caltech.edu/ipac/iras/hires\\_over.html](http://www.ipac.caltech.edu/ipac/iras/hires_over.html). This section emphasizes the unique problems encountered in the IGA production.

#### 3.1. Overview of the Production Pipeline

*IRAS* detector data, known as CRDD (Calibrated, Reconstructed Detector Data), grouped in  $7^\circ \times 7^\circ$  plates, reside in the “*Level 1 Archive*” at IPAC. The first step in the pipeline for mass production of HIRES images is to extract data covering a specific field from the archive and then perform calibration and various other preprocessing. We take the  $7^\circ \times 7^\circ$  preprocessed and calibrated plates and use the algorithm described in Section 3.3 to subtract the zodiacal background emission. This step requires the corresponding ISSA image as supplemental input (SmLAUN in Fig. 1, Section 3.3).

Following the calibration and zodiacal subtraction, the detector files are broken into  $1.4^\circ \times 1.4^\circ$  fields, and reprojected into Galactic coordinates (from equatorial) if required, with field centers separated by 1 degree (BrkDet in Fig. 1, Section 3.4). The factor-of-two overlap is a conservative insurance against discontinuity across field boundaries (see Section 4.7), as local destriping and different flux bias (see Sec. 3.5) will be applied to each

small field. The  $1.4^\circ \times 1.4^\circ$  size is also the maximal field size with complete coverage allowed within one Level 1 plate, given the 2 degree redundancy of the plates and arbitrary location and orientation of the small field relative to the Level 1 plate. Figure 2 illustrates the overlapping IGA fields, and the geometry and orientation of the Level 1 plates that determine the allowed IGA field size.

All operations described above are carried out on workstations. The small field ( $1.4^\circ \times 1.4^\circ$ ) detector files are then processed into HIRES images, which is done on the Intel Paragon supercomputer. The basic algorithm for image reconstruction is described in Section 3.2. For parallelization strategy and details of the destriping algorithm, see Paper I.

### 3.2. The Maximum Correlation Method

Starting from a model of the sky flux distribution, the HIRES MCM algorithm folds the model through the *IRAS* detector responses, compares the result track-by-track<sup>1</sup> to the observed flux, and calculates corrections to the model. One important characteristic is that the standard MCM algorithm conserves flux. We give a brief description of the MCM algorithm following the formalism and notations of Aumann, Fowler, and Melnyk (1990) .

Given an image grid  $f_j$ , with  $n$  pixels  $j = 1, \dots, n$  and  $m$  detector samples (*footprints*) with fluxes  $D_i : i = 1, \dots, m$ , whose centers are contained in the image grid, an image can be constructed iteratively from a zeroth estimate of the image,  $f_j^0 = \text{const.} > 0$  for all  $j$ . In other words the initial guess is a uniform, flat, and positive definite map. For each footprint, a correction factor  $C_i$  is computed as,

$$C_i = D_i/F_i, \tag{1}$$

where

$$F_i = \sum_j r_{ij} f_j, \tag{2}$$

and  $r_{ij}$  is the value of the  $i$ th footprint's response function at image pixels  $f_j$ . Therefore  $F_i$  is the current estimate of the  $i$ th footprint's flux, given image grid  $f_j$ .

A mean correction factor for the  $j$ th image pixel is computed by projecting the correction factor for the footprints into the image domain:

$$c_j = [\sum_i (r_{ij}/\sigma_i^2) C_i] / [\sum_i (r_{ij}/\sigma_i^2)]. \tag{3}$$

---

<sup>1</sup>Track, also called *leg* or *scanline*, refers to the set of data samples collected consecutively by one detector moving across a given field.

The weight attached to the  $i$ th correction factor for the  $j$ th pixel is  $r_{ij}/\sigma_i^2$ , where  $\sigma_i$  is the *a priori* noise assigned to the  $i$ th footprint.

The  $k$ th estimate of the image is computed by

$$f_j^{(k)} = f_j^{(k-1)} c_j. \quad (4)$$

In practice when the footprint noise  $\sigma_i$  is not easily estimated, an equal noise value for all footprints is assumed, and the MCM is identical to the Richardson-Lucy algorithm (Richardson 1972, Lucy 1974).

Table 1 shows the quantities represented by the ancillary maps (Aumann, Fowler, & Melnyk 1990). For more detailed information on the HIREs ancillary maps, see [http://www.ipac.caltech.edu/ipac/iras/hires\\_maps.html](http://www.ipac.caltech.edu/ipac/iras/hires_maps.html). The correction factor variance (CFV) map gives an estimate of the level of convergence at a certain pixel, measuring the agreement of correction factors projected onto it from different detector footprints. The photometric noise (PHN) map signifies the photometric noise at a pixel, propagated from noise in the detector measurements. The coverage (CVG) map is the sum of the response function grids of all footprints within the field. The detector track (DET) map registers the footprint centers and helps visualize the detector scanning pattern. Artifacts due to low coverage may be diagnosed using the coverage maps. The remaining ancillary maps provide diagnostics for other less frequent artifacts.

The effective beam size in HIREs images depends on the response function and sample density in a complicated fashion, and may vary by factors of three over distances of several arcminutes (Fowler & Aumann 1994). In order to estimate the beam size at any given position and to see typical variation over the field, “beam sample maps” (BEM) are provided. These are produced from simulated detector data based on actual coverage geometry, with the simulation scene being a collection of spike sources against a smooth background. An image of the reconstructed spikes (beam sample map) is generated with all the same processing options as the actual image.

### 3.3. Subtraction of Zodiacal Emission

Zodiacal dust emission is a prominent source of diffuse emission in the *IRAS* survey. The zodiacal contribution to the observed surface brightness depends on the amount of interplanetary dust along the particular line-of-sight, an amount which varies with the Earth’s position within the dust cloud. Consequently, the sky brightness of a particular location on the sky as observed by *IRAS*, changes with time as the Earth moves along its orbit around the Sun. The different zodiacal emission level in different scanlines, if not

subtracted, can cause step discontinuities in the images if adjacent patches of sky were observed at different times.

A physical model of the zodiacal foreground emission based on the radiative properties and spatial distribution of the zodiacal dust was developed by Good (1994). The *IRAS* Sky Survey Atlas (ISSA; Wheelock et al. 1994) made use of this model and subtracted the predicted zodiacal emission from the detector data before co-adding them.

However, the *IRAS* detector data which serve as input to the IGA and other *IRAS* image products, still contain zodiacal emission. A preprocessing method has been developed to bring the raw detector data flux to a common level with the ISSA images, effectively subtracting the zodiacal emission component (Paper I). Nearby ISSA images ( $12.5^\circ \times 12.5^\circ$ ,  $1.5'$  pixels) were reprojected and mosaicked to cover the same field-of-view as a Level 1 plate ( $7^\circ \times 7^\circ$ ,  $1'$  pixels). A set of simulated data is then calculated from the mosaicked image, by running the actual *IRAS* scan pattern through this image,

$$F_i^{\text{ISSA}} = \sum_j r_{ij} f_j^{\text{ISSA}} \quad (5)$$

The difference between these simulated data and the real data is then used to determine the local zodiacal emission

$$D_i^{\text{ZODY}} = \text{median}(D_i - F_i^{\text{ISSA}}) \quad (6)$$

where the median is taken for nearby footprints in the same scanline with a total spatial range of  $1^\circ$ . The zodiacal component is then subtracted

$$D_i^{\text{NEW}} = D_i - D_i^{\text{ZODY}} \quad (7)$$

and the new data output for use in image construction.

Because of the large spatial scale used in Eq. (6), the resulting zodiacal emission flux,  $D_i^{\text{ZODY}}$ , varies smoothly with a characteristic scale of  $\sim 1^\circ$ . Therefore the zodiacal subtraction process does not interfere with the high spatial frequency information inherent in the raw data, which is needed for the image reconstruction and resolution enhancement.

### 3.4. Coordinate Transform and Reprojection

Each Level 1 plate covers a field of view of  $7^\circ \times 7^\circ$ , using a projection center local to the plate. The positions of detector footprints are stored in equatorial coordinates using

Cartesian projection (Greisen & Calabretta 1996; FITS keywords RA---CAR, DEC--CAR, B1950):

$$\begin{aligned} x &= \phi, \\ y &= \theta, \end{aligned} \tag{8}$$

where  $\theta$  and  $\phi$  are angles in the native coordinate system (Euler angles with respect to local great circles). Each Level 1 plate has its own projection center ( $C$  in Fig. 3).

For the IGA, the Cartesian projection (FITS keywords GLON-CAR and GLAT-CAR) with reference point at the Galactic center is convenient, in which case  $l$  and  $b$  map linearly to  $x$  and  $y$ .

To transform the equatorial coordinates of footprints stored in the Level 1 archive to Galactic, the following steps are done in BrkDet. For each footprint centered at  $P$ , a unit vector  $OP$  is computed in the equatorial system, using RA and Dec of the projection center  $C$ , and the  $x$  and  $y$  of  $P$  in the Cartesian projection system centered at  $C$ . Then the unit vector is rotated to the Galactic system, and  $l$  and  $b$  are obtained (see Fig. 3). Coordinates and fluxes of footprints falling in each  $1.4^\circ \times 1.4^\circ$  field of view are grouped together and written out for the final image reconstruction step.

The tilt angle for each scanline, which is necessary for calculating the response function grid during image reconstruction, also needs to be redetermined in the Galactic coordinate system. For a scanline with  $n$  footprints located at  $(x_i, y_i), i = 1, \dots, n$ , this was done by fitting a straight line through the  $x$  and  $y$  values, by minimizing  $\sum_i \Delta_i^2$ , where  $\Delta_i$  is the distance from footprint  $i$  to the line. This gives the estimate for the tilt angle  $\Phi$ , measured relative to the  $x$  axis

$$\Phi = \frac{1}{2} \arctan \frac{2 \sum_i x_i y_i - \bar{x} \bar{y}}{\sum_i x_i^2 - \bar{x}^2 - \bar{y}^2 + \bar{y}^2} \tag{9}$$

where

$$\begin{aligned} \bar{x} &= \sum_i x_i / n \\ \bar{y} &= \sum_i y_i / n. \end{aligned} \tag{10}$$

For the molecular cloud fields (Orion,  $\rho$  Ophiuchus, and Taurus-Auriga), equatorial coordinates were used (FITS keywords RA---CAR and DEC--CAR, B1950), and the Level 1 archive geometry was retained (no reprojection of the footprint data was performed). Each Level 1 plate ( $7^\circ \times 7^\circ$  on  $5^\circ$  centers) was divided into  $3 \times 3$  subfields of  $2.5^\circ \times 2.5^\circ$  each, on  $2^\circ$  centers, with the projection center the same as the Level 1 plate center. Therefore the subfield images belonging to the same Level 1 plate are mosaickable without the need of



reprojection, but special care needs to be taken when mosaicking subfields from different Level 1 plates. The use of Cartesian projection for Equatorial coordinates is closest to the native format of the *IRAS* data, but differs from the more commonly used *-SIN* projection by about 0.5 pixel at the edge of a Level 1 plate.

### 3.5. Issues Related to Flux Bias

Astronomical images often contain backgrounds which need to be subtracted from the source of interest, such as instrumental offsets, sky backgrounds, or in the case of the *IRAS* data, zodiacal light or diffuse Galactic backgrounds. This means that the zero level of an image depends on the specific application for which part of the signal is considered source or background. Taking advantage of this arbitrary nature of the background level, many resolution enhancement schemes add a constant value to the image which is chosen to optimize the performance of the algorithm.

Because of the nonlinear nature of the MCM algorithm, the spatial resolution achieved by HIRES processing is not invariant under application of an additive *flux bias*:

$$D_i \longrightarrow D_i + F_{\text{BIAS}}. \quad (11)$$

Generally, the closer to zero the data, the higher the resolution obtained. Alternatively, the more iterations, the higher the resolution obtained. However, the MCM algorithm is unstable to negative data values. The optimum performance is obtained by using data with small but nonnegative values. Therefore, to maximize both spatial resolution and throughput, a flux bias is computed and applied before the image reconstruction step, to bring the data close to zero in order to achieve higher resolution at a given iteration. Since the flux bias is only important during the image processing step, the applied flux bias is subtracted from the result image so that the surface brightness of the output image matches the original data.

For IGA processing, the flux bias is calculated in the BrkDet step, using the negative of the first percentile from the flux histogram in each  $1.4^\circ \times 1.4^\circ$  field. In other words, the first percentile is used as the zero point in subsequent HIRES processing. The detector data having fluxes below the first percentile are discarded, since negative data cause instabilities in the algorithm.

## 4. Characteristics of the Images

In this section “IGA(1)” denotes the 1st iteration IGA images, and “IGA(20)” the 20th. The resolution, photometric accuracy, positional accuracy, surface brightness accuracy, mosaic property, and residual hysteresis effect of the images are discussed and quantified.

### 4.1. Resolution

The diffraction limit of the *IRAS* 0.6m telescope is  $50''$  and  $84''$  at 60 and 100 microns, respectively. The effective beam of the coadded *IRAS* data is much larger, typically  $2.0' \times 4.7'$  at  $60 \mu\text{m}$  and  $3.8' \times 5.4'$  at  $100 \mu\text{m}$  due to the large and rectangular *IRAS* detectors. The MCM algorithm makes use of the geometric information in the large number of redundant tracks with differing scan angles to extract higher spatial resolution, which in some cases can approach the diffraction limit of the telescope (Rice 1993). The effective beam size in HIRES images depends on the response function and sample density in a complicated fashion. The resolution also depends on the magnitude of the point source relative to the effective background (see also Sec. 3.5).

The spatial resolution of a given field can be estimated from the corresponding BEM maps produced from simulated data (see also Sec. 3.2 and Table 1). To generate the BEM maps artificial point sources are added to the smoothed data, which then undergo HIRES processing. Specifically, point sources are identified and removed from IGA(20) image: the image, further smoothed, provides a model background to which regularly spaced ( $12'$ ) point sources are added. The magnitude of the planted point source spikes is adjusted according to the dynamic range of the IGA(20) image: the pixel intensity is set to  $20 \times (99\% \text{quantile} - 50\% \text{quantile})$  of the IGA image histogram (plus the background). The numerical value of 20 approximately converts the flux from per unit beam to flux per unit pixel. This arbitrary choice of flux is meant to represent a typical point source which is strong enough with respect to the local Galactic background to benefit from high-resolution processing. A set of simulated data is then generated from the artificial image, from which the BEM map is reconstructed through HIRES. A Gaussian profile is fitted to the reconstructed point sources in the BEM maps, and the FWHM along the major and minor axes are taken as the measure for the achieved resolution.

The typical resolution of the IGA(20) images is  $1.0' \times 1.7'$  at  $60 \mu\text{m}$  and  $1.7' \times 2.2'$  at  $100 \mu\text{m}$ , which represents a substantial improvement over the coadded images. Figure 4 demonstrates the dependence of the resolution upon longitude across the Galactic plane. The plotted major and minor axis FWHM were averaged over latitude. Two obvious dips

are seen in the major axis curves, both in 60 and 100  $\mu\text{m}$ , near  $l = 100^\circ$  and  $l = 280^\circ$ . These two areas in the Galactic plane featured near-perpendicular intersecting scanlines in the *IRAS* survey, and the extra geometric information in the data gives rise to the increased resolution.

To investigate the dependence of resolution on source strength relative to background level, BEM maps were generated for simulated point sources ranging from 1 to 10,000 Jy in strength. The background intensity level determined for the test field near  $l = 120^\circ$  was 53.94 MJy/sr and 165.05 MJy/sr at 60 and 100  $\mu\text{m}$ , respectively. Integrated over the effective solid angle of the *IRAS* detectors,  $6.25 \times 10^{-7}$  and  $13.54 \times 10^{-7}$  sr, the detector fluxes due to the local background become 33.7 and 223 Jy, respectively. To find the effective background during HIRES processing, the flux bias value from the FITS header (see Sec. 3.5) can be converted from  $\text{W m}^{-2}$  to Jy through division by the conversion factors  $2.58 \times 10^{-14}$  or  $1.00 \times 10^{-14}$  at 60 and 100  $\mu\text{m}$ , respectively, and then subtracted from the corresponding local background flux. In this test case, zero flux bias was used, giving simply 33.7 and 223 Jy for the processing background at 60 and 100  $\mu\text{m}$ , respectively. We emphasize that the spatial resolution depends on the effective background level *during* HIRES processing, namely the local background minus the flux bias value. A quick way to estimate the processing background in IGA images is to find the minimum intensity value in the image (which will be close to the flux bias value) and then subtract it from the local background. If necessary, convert from intensity to flux in Jy using the detector solid angles given above.

The results plotted in Figure 5 show that the IGA(20) resolution is at least a factor of two better than the coadded IGA(1) resolution. Also, the resolution significantly improves for point sources stronger than the processing background of 33.7 and 223 Jy at 60 and 100  $\mu\text{m}$ , respectively. Furthermore, when the source-to-background contrast reaches about 20, the achieved resolution becomes insensitive to the background. The resolution in other fields/regions should behave in the same qualitative fashion when the local processing background is computed as above.

Figure 5 shows the additional effect that offset compensation destriping (Paper I, also see Sec. 5.1) gives comparable but slightly poorer resolution than standard HIRES destriping, especially along the major axis (cross scan) direction.

The number of iterations also effects the spatial resolution, although in practice most of the improvement in spatial resolution is gained within the first 10 iterations. For IGA processing, 20 iterations was chosen in a tradeoff between speed of processing and artifact development versus spatial resolution. However, for strong sources, regions of high coverage, or regions with favorable scanline geometry, data reprocessing with additional iterations

gives better spatial resolution (Rice 1993, Hurt & Barsony 1996).

In addition, note that the beams of the IGA images are not Gaussian. The most prominent deviation of the beam from a 2-dimensional Gaussian is due to the ringing artifact (Section 5.2). Rice (1993) gives a detailed account of the HIRES beams.

## 4.2. Photometric Accuracy

To test the photometric accuracy thirty-five relatively isolated point sources (with a well-defined background) were selected. All sources have flux  $> 10$  Jy and are spatially unresolved as measured by the Correlation Coefficient (CC) flag in the *IRAS* Point Source Catalog (1988). Fluxes were measured using an aperture photometry program developed at IPAC, in which the median pixel intensity within an annulus (radius  $5'$ – $7'$ ) centered at the point source position (taken from the PSC) is taken as the background intensity. Two estimates of the point source flux are then made, using the total fluxes within  $5'$  and  $7'$  radius from the PSC position (minus the background intensity  $\times$  the number of pixels). For sources chosen for the photometry test, these two values are usually sufficiently close to each other to indicate a well-defined background level. The average of these two values is taken as the point source flux from the IGA image, and compared against the value from the PSC. The computed fluxes are given in Table 2, while Table 3 summarizes the statistical correlation between IGA and PSC flux values.

An overall offset (12%) between the IGA(1) and PSC fluxes is seen at  $60 \mu\text{m}$  which is, however, not present at  $100 \mu\text{m}$  (1%). One possible explanation for the  $60 \mu\text{m}$  offset is the different data calibration used, specifically the hysteresis correction. The IGA and other recent *IRAS* image products are based on the final *IRAS* Pass 3 calibration, described in detail in the ISSA Explanatory Supplement (Wheelock et al. 1994). This calibration includes a hysteresis correction at both  $60$  and  $100 \mu\text{m}$  (see Sec. 4.8). The PSC, however, is based on *IRAS* Pass 2 CRDD data, which were corrected after the fact to the Pass 3 calibration. One significant difference is the way in which hysteresis was treated: the PSC applied a hysteresis correction only at  $100 \mu\text{m}$  (*IRAS* Catalogs and Atlases: Explanatory Supplement 1988). The lack of hysteresis correction at  $60 \mu\text{m}$  for PSC sources, particularly important for the Galactic plane where hysteresis is strongest, provides one explanation for why there is a systematic offset at  $60 \mu\text{m}$ , but not at  $100 \mu\text{m}$ , between the IGA(1) and PSC fluxes.

In addition, Table 3 shows there is a growth in flux from the 1st to 20th iteration which is small (2%) for the  $60 \mu\text{m}$  band, but significant (10%) for the  $100 \mu\text{m}$  band. Analysis

shows that the effect is caused by the depression of the background due to the ringing artifact. In the Galactic plane, where the background emission is strong and structured, the largest contributor to the flux uncertainty is the background determination (Fich & Terebey 1996). The total flux within the selected aperture is comprised of the source flux plus a background contribution (background  $\times$  area). For the photometry sample, the ratio of background flux to source flux is 1.8 at 60  $\mu\text{m}$  and 6.7 in the 100  $\mu\text{m}$  band. In addition, the background level systematically decreases on average by 1.7% for 60  $\mu\text{m}$ , and 1.8% at 100  $\mu\text{m}$  due to ringing in the 5' – 7' annulus. This leads to an apparent flux increase from 1 to 20 iterations of  $1.8 \times 1.7\% = 3\%$  at 60  $\mu\text{m}$  and  $6.7 \times 1.8\% = 12\%$  in the 100  $\mu\text{m}$  band, which agrees with the results of Table 3.

To compensate for the systematically low background levels we recomputed the IGA(20) source fluxes using IGA(1) background levels. The resulting fluxes show no systematic offset (mean of IGA(20)/IGA(1) = 0.99) and better correlation with IGA(1) fluxes (standard deviation = 0.10). This technique of using IGA(1) backgrounds to calculate IGA(20) fluxes is recommended whenever the most stable and accurate photometry is required.

The growth in flux found for IGA point sources is not a universal property of HIRES processing. In a HIRES study of interacting Galaxy pairs, Surace et al. (1993) found HIRES fluxes systematically decreased by 20% from iteration = 1 (FRESCO) to iteration = 20, a result they attributed to the small extended nature of the sample. Since the MCM algorithm fundamentally conserves flux, the effect is either due to a systematic increase in the background, or to redistribution of flux outside the photometric aperture. The use of the IGA(1) background to compute the IGA(20) flux is a technique that can help determine the cause of such systematic trends.

Figure 6 plots the dependence of (IGA(20) flux / PSC flux) on the PSC flux. There is no trend with source flux, apart from the previously discussed offsets.

### 4.3. Size Dependent Flux Correction

The estimation of the flux for extended sources ( $> 4' - 40'$ ) may involve a size dependent flux correction, also known as the AC/DC correction. The *IRAS* detectors had a dwell-time dependent responsivity change. Hence, the gain changes as a function of source size: at the *IRAS* survey speed of 3.85 arcmin/s, the gains leveled off for structure on the order of 40' in extent. This effect was band-dependent and largest at 12  $\mu\text{m}$ . Thus, there are two calibrations for the *IRAS* data, the calibration appropriate for point sources, known

as the AC calibration, and the calibration appropriate to very extended structure, known as the DC calibration. To bring point source fluxes measured from DC-calibrated products to the AC (same as the PSC) calibration, the fluxes must be divided by 0.78, 0.82, 0.92 and 1.0 at 12, 25, 60 and 100  $\mu\text{m}$ , respectively. The IGA uses the AC calibration, while the ISSA images are on the DC scale.

Point source fluxes obtained by aperture photometry with appropriate background subtraction on AC calibrated images such as the IGA should be consistent with the PSC. However, neither calibration is strictly correct for structure on spatial scales intermediate between point sources and  $30'$  in size. Intermediate-scale corrections and uncertainties can be estimated from the plots in the *IRAS* Catalogs and Atlases: Explanatory Supplement (1988).

#### 4.4. Calibration Uncertainty

The flux measurement uncertainty derived from point sources (Table 3) for the IGA(1) images is 11% and 16% at 60 and 100  $\mu\text{m}$ , respectively. Given the isolated nature of the sources, these uncertainties represent a best case. A better estimate of the measurement uncertainty in more complex regions is given by Fich & Terebey (1996), who find 17% and 18% for the flux measurement uncertainty of at 60 and 100  $\mu\text{m}$ , respectively, for a sample of outer Galaxy star forming regions.

In some cases, systematic instrumental effects also contribute significantly to the flux uncertainty. The *IRAS* calibration for point sources is accurate, albeit affected by residual hysteresis at 60 and 100  $\mu\text{m}$  in the Galactic plane. As described in the previous section, there is a 12% systematic uncertainty at 60  $\mu\text{m}$  between the IGA(1) and PSC. At 100  $\mu\text{m}$  the uncertainty due to residual hysteresis is less than 5% over most of the Galactic plane, but approaches a maximum of 20% near the Galactic center.

For small but extended ( $5' - 20'$ ) sources the situation is complex. The size-dependent flux correction, the so-called AC/DC effect (see Sec. 4.3) is typically about 10% or less. However the detector response is not well-behaved for bright extended sources: above 100 Jy the *IRAS* Explanatory Supplement quotes uncertainties of 30% at 60  $\mu\text{m}$  and 70% at 100  $\mu\text{m}$  (*IRAS* Catalogs and Atlases: Explanatory Supplement 1988).

Prominent in the IGA is diffuse Galactic emission associated with HI, which varies on a scale of a few degrees. The *IRAS* – COBE comparison gives an indication of the calibration uncertainty. Over angular scales larger than  $10^\circ$  the *IRAS* calibration differs systematically from that of COBE by 13% and 28% at 60 and 100  $\mu\text{m}$ , respectively (Wheelock et al. 1994).

The ISSA survey was used as large scale surface brightness truth table for the IGA. This implies that defects or uncertainties introduced by the ISSA processing extend to the IGA as well (see Sec. 5.4). At 60 and 100  $\mu\text{m}$ , residuals associated with zodiacal emission model can approach 1 – 2 MJy/sr in the ecliptic plane (Galactic center and anti-center directions), but are typically far less (e.g. Fich & Terebey 1996). For more information consult the ISSA Explanatory Supplement (Wheelock et al. 1994).

#### 4.5. Positional Accuracy

*IRAS* Point Source Catalog positions were used as truth tables for a positional accuracy test of the IGA. Positions were computed for the same sample of thirty-five sources used in the photometry comparison. For each source, a circular area with radius  $5'$  was defined (centered at the PSC position), and the area's flux-weighted centroid was taken as the point source position implied by the IGA image and compared against the PSC position.

Table 4 shows the result of the comparison. For the 60  $\mu\text{m}$  band, the distances between the IGA position and PSC position have an average of  $7.6''$  and standard deviation  $5.6''$ , while for 100  $\mu\text{m}$ , there is a  $7.1'' \pm 4.1''$  difference.

The PSC reports error ellipses corresponding to the 95% confidence level for source positions. The major and minor axes of the error ellipse correspond approximately to the cross- and in-scan directions. For each source, we projected the IGA position along the major and minor axes of the error ellipse centered at the PSC position. The mean deviations from the PSC position were found to be similar along the major and minor axis directions, and do not scale with the length of the major and minor axes. This indicates the positional errors produced by the MCM algorithm are due to nonsystematic effects unrelated to the *IRAS* scan pattern and detector geometry.

#### 4.6. Surface Brightness Accuracy

To test the surface brightness of the zodiacal light subtracted IGA images, they were rebinned to match the ISSA geometry and compared pixel-by-pixel against the ISSA images. The standard deviation of the  $1.5'$  pixel-by-pixel difference is less than 6% for IGA(1) vs. ISSA, and less than 12% for IGA(20) vs. ISSA. No systematic offset was found between the IGA and ISSA data. See Paper I for details.

#### 4.7. Mosaic Property

The geometry of the IGA images allows them to be mosaicked without any reprojection, hence no smoothing is required and the original resolution can be retained in the mosaicked images. To reduce edge discontinuities, the images should first be cropped to  $1^\circ \times 1^\circ$  from  $1.4^\circ \times 1.4^\circ$  with the centers unshifted before mosaicking. No offset needs to be applied to the different subfields. In most cases the mosaicked image is seamless to the human eye.

Quantitatively, within a chosen Level 1 plate in the W3, W4, and W5 region, pixel intensity ratios were calculated for 1-pixel wide edges covered by neighboring subfields after cropping the subfields to slightly larger than  $1^\circ \times 1^\circ$ . Table 5 summarizes the intensity ratio statistics for both the 1st and 20th iteration images. A total of 10122 pixels in 42  $1^\circ$  edges were used in the calculation. For 20th iteration images, the standard deviation of the ratio amounts to 0.51% and 0.23% for band 3 (60  $\mu\text{m}$ ) and 4 (100  $\mu\text{m}$ ) respectively. Intensity ratio statistics were also calculated for cross-Level 1-plate boundaries, using a total of 8194 pixels in 34  $1^\circ$  edges. Again for 20th iteration images, the standard deviations are 1.5% and 0.46% for band 3 and 4. The match is worse than that of intra-plate edges, since the zodiacal subtraction was done separately for each Level 1 plate (see Sec. 3.3).

The better boundary match (smaller deviation) at band 4 can be understood from the poorer resolving power of HIRES at band 4 than at band 3, which decreases the resolution difference between subfields caused by the different flux bias levels used in the image reconstruction process (see Sec. 3.5).

#### 4.8. Residual Hysteresis

The *IRAS* detectors showed photon induced responsivity enhancement, known as the hysteresis effect, especially in the 60 and 100  $\mu\text{m}$  bands. The effect is prominent when the scanlines pass the Galactic plane (e.g. *IRAS* Catalogs and Atlases: Explanatory Supplement 1988, Chap. VI) and thus a concern for the IGA survey. The final *IRAS* Pass 3 calibration, on which both the IGA and ISSA are based, employed a physically based detector model to correct for the hysteresis. However, the technique could not correct variations that were more rapid than  $\sim 6^\circ$  in spatial scale (Wheelock et al. 1994, Chap. III). This section quantifies the residual hysteresis near the Galactic plane in the ISSA data, which should also describe the residual hysteresis present in the IGA.

In the *IRAS* survey, a given region can be covered by up to 3 scans carried out at different times, known as Hours CONFIRMING (HCON) scans. HCON 1 and HCON 2 were



separated by up to several weeks, while HCON 3 was taken roughly 6 months later.<sup>2</sup> This meant HCON 3 usually passed the Galactic plane along the opposite direction of HCON 1 and 2, since *IRAS* followed a Sun-synchronous orbit and the telescope always pointed approximately 90° away from the Sun.

Figure 7 illustrates the effect on computed flux values from the different HCONs that is caused by the photon induced responsivity change. At the starting and ending points of a scan, *IRAS* detectors were lit up by an internal calibration flash, which anchored the responsivity of the detectors at these two points. In the early calibration schemes, the response was assumed to change linearly between the two calibration flashes, which imperfectly tracks the true detector response when the scan passes through bright regions like the Galactic plane (Fig. 7a). Figure 7b illustrates the resulting deviation of the computed fluxes from true values. For example, the computed flux of a 1 Jy source differs from 1 Jy in a systematic way that depends both on galactic latitude and the scanning direction. Figure 7c shows the ratio of fluxes determined from descending and ascending scans; the ratio should equal one for perfectly calibrated data.

To quantify the residual hysteresis effect in the ISSA images, ISSA images made from HCON 1 and 3 were compared at  $l = 0^\circ, 10^\circ, 20^\circ, 60^\circ, 120^\circ, 180^\circ, 240^\circ, 300^\circ, 340^\circ,$  and  $350^\circ$ . Images covering  $\pm 5^\circ$  latitude and  $\pm 2.5^\circ$  longitude were first smoothed with a  $4.5'$  boxcar kernel, roughly the ISSA resolution, and then summed over  $5^\circ$  longitude intervals to increase signal to noise. Pixel intensity ratios (HCON 1 / HCON 3) were computed then averaged over each  $5^\circ (l) \times 4.5' (b)$  box.

Figures 8 and 9 plot the average intensity (left column) and HCON1/HCON3 intensity ratio (right column) versus Galactic latitude. Plots made versus Galactic latitude are sufficient for our purpose, although strictly speaking ecliptic latitude better represents the *IRAS* scanning direction. The hysteresis signature is seen clearly near  $l = 0^\circ$  with an amplitude of about 20% at  $100 \mu\text{m}$ . As expected, the peak of the average intensity plot corresponds to the appearance of the hysteresis signature in the ratio plot. Hysteresis may also be present in the  $l = 60^\circ$  and  $300^\circ$  graphs but below the 5% level. Other small ( $< 5\%$ ) but systematic variations in the ISSA ratio are likely due to destriping differences. Figure 10 shows the maximum and minimum HCON1/HCON3 intensity ratio found at each longitude. At  $100 \mu\text{m}$  and within  $60^\circ$  of the Galactic center, residual hysteresis becomes larger than systematic differences due to destriping and noise.

---

<sup>2</sup>Most (96%) of the sky was covered by at least two HCONs, and 2/3 of the sky was covered by three HCONs.

## 5. Artifacts

For general descriptions of artifacts produced by HIRES processing, see [http://www.ipac.caltech.edu/ipac/iras/hires\\_artifacts.html](http://www.ipac.caltech.edu/ipac/iras/hires_artifacts.html).

### 5.1. Striping Artifacts

Stripes were formerly the most prominent artifacts in HIRES images. HIRES takes as input the *IRAS* detector data, and if not perfectly calibrated, would try to fit the gain differences in the detector scans by a striped image. The striping builds up in amplitude and sharpness along with the HIRES iterations, as the algorithm refines the “resolution” of the stripes.

An algorithm was developed to eliminate the striping artifacts. The basic technique involved is to estimate gain variations in the detectors and compensate for them within the image reconstruction process. Observation of the Fourier power spectrum of the resulting images shows that the algorithm eliminates the striping signal after roughly ten iterations. Therefore striping artifacts have been virtually eliminated from the IGA images. See Paper I for details and examples.

### 5.2. Ringing Artifacts

“Ringing” is a prominent artifact in the IGA images. When a point source is superimposed on a non-zero background, the artifact known as *ringing* or ripples appears in many image reconstruction algorithms. In Fourier language, the reconstruction process tries to make the image agree with the true scene in the low spatial frequency components (data constraint), without access to the infinitely high spatial frequencies inherent in the point source scene. The magnitude of the ringing depends on the strength of the point source, the level of the residual background intensity (after the application of flux bias), and the detector scan pattern. For nonlinear algorithms (such as MCM) the dependence is complicated and difficult to quantify.

The ringing artifact adds uncertainty to the level of background emission around point sources, thus hindering photometric accuracy (see Sec. 4.2). The ringing may also interfere with the lower intensity structures present in the background. Numerous approaches have been developed in the field of astronomical image reconstruction to overcome the difficulty (Frieden & Wells 1978, Lucy 1994, Bontekoe et al. 1994).

At the time when IGA image production started, no satisfactory algorithm was found for the purpose of ringing suppression for the atlas (see Paper I) which preserves photometric integrity and does not require extra prior knowledge (such as the positions and fluxes of point sources) as input. Therefore the IGA images were produced with the standard MCM algorithm (plus gain compensation destriping), which has the advantage of proven flux conservation. Ringing thus remains as the only major artifact in the IGA images.

Figure 11 demonstrates the ringing artifact around several point sources. At the 1st iteration, the point sources are poorly resolved and no ringing is seen. At the 20th iteration, low intensity rings (the shape of which is roughly elliptical and determined primarily by the detector response functions) surround the point sources. Further away from each point source, a brighter ring is usually visible.

An iterative algorithm was later developed (but too late for IGA production) which aims to maximize the relative Burg entropy between modeled and measured data (Cao 1997, Cao et al. 1997). The algorithm was run on several test fields, and was found to suppress ringing effectively and give good photometry. A partial convergence proof has also been found. The algorithm has been applied to the bright infrared star  $\alpha$  Ori with good results (Noriega-Crespo et al. 1997). At  $60 \mu\text{m}$  the morphology of a  $7'$  sized bow-shock shows dramatic improvement. On a smaller scale the ringing is suppressed to the level where diffraction spikes surrounding the star become visible.

### 5.3. Glitches

Glitches are caused by hits on individual detectors by cosmic rays or trapped energetic particles. The IPAC utility LAUNDR passes the flux values in each scanline through two filters, one detecting point sources and one glitches. If the ratio of the power in the point source filter to that in the glitch filter is greater than a certain threshold (default is 1), the phenomenon is taken to be a point source, otherwise a glitch.

In a few regions found by visual inspection, glitches were mistaken as point sources and leaked into the image reconstruction stage. In such cases reprocessing with a higher point source to glitch power threshold in LAUNDR sufficed to eliminate the artifact. However, it is not guaranteed that all such artifacts have been uncovered.

Remaining glitches in the IGA are rare but fairly easy to identify. In 1st iteration images, a glitch traces out the shape of a single detector response function, and possesses a different profile from that of a point source (a glitch being narrower than a point source).

At the 20th iteration, a glitch would take on a “broken-up” shape, showing structures finer than the physically achievable resolution, as shown in Figure 12, while a point source is usually characterized by the ringing artifact. These differences provide a way to distinguish between real point sources and glitches in the images.

#### 5.4. Discontinuities

The ISSA images employed both global and local destriping techniques, and the local destriping left some amount of intensity discrepancy between adjacent ISSA plates (Wheelock et al. 1994).

When reprojecting and mosaicking the ISSA images to the Level 1 geometry (against which the detector data are calibrated and zodiacal emission removed), care was taken to adjust the cropping of neighboring ISSA plates to minimize the discontinuity. In a small number of cases, however, some discontinuity remained which eventually affected the final IGA image. The discontinuity is not seen in the 1st iterations, but is sharpened and visible in the 20th. Less than 0.5% of all the  $1.4^\circ \times 1.4^\circ$  subfields are affected by this artifact. Figure 13 shows one instance of the discontinuity across a subfield ( $60 \mu\text{m}$ , 20th iteration). The difference in intensity is approximately 5 MJy/sr.

The different flux bias values used in different  $1.4^\circ \times 1.4^\circ$  fields also affects the mosaicking property of nearby images, since different resolutions are achieved in the overlap region from the two images. See Section 4.7 for a detailed discussion.

#### 5.5. Coverage Artifacts

After the processing of the mini-survey ( $-1.7^\circ < b < 1.7^\circ$ ), it was found that the data processing window was too small, causing coverage depletion, and therefore unreliable structure near window boundaries. A border of at least  $5'$  should be cropped from images within the mini-survey. For the extended survey ( $1.3^\circ < |b| < 4.7^\circ$ ), a larger window ( $1.67^\circ \times 1.67^\circ$ ) was used in BrkDet to avoid coverage depletion.

The use of a flux bias (see Sec. 3.5), to bring the data closer to zero during processing, and thereby increase throughput, was necessary but led to a subtle artifact. The IGA processing subtracted a flux bias from the data corresponding to the first percentile from the flux histogram. Data below the threshold were discarded. This procedure effectively assumes the lower 1% of the data are due to noise in the flux values, which is not always justified. In fields which had structured backgrounds, particularly at  $100 \mu\text{m}$ , it was found

that discarding data resulted in severe coverage depletion at the intensity minimum of an image. All images where the coverage fell below a value of 5 in the coverage map were reprocessed with a smaller flux bias. However problems, such as anomalous structure near the image intensity minimum, may remain. The ancillary CVG map can help diagnose problems associated with inadequate coverage.

The HIRES algorithm can cause systematic positional shifts if the coverage changes abruptly. In cases where positional accuracy is important, the CVG maps should be checked for the presence of discontinuities or steep ( $< 5'$ ) coverage gradients. The sense of the artifact is to shift source positions systematically down and along the coverage gradient.

## 6. Example Images

To illustrate the image quality of the IGA, mosaics at  $60 \mu\text{m}$  of a restricted latitude range ( $-1.7^\circ < b < 1.7^\circ$ ) were made for regions between Galactic longitude  $280^\circ$  and  $80^\circ$  (approximately 16% of the total area covered by the atlas), and are shown in Fig. 14, 15, 16, and 17. Most of the emission is from stellar heated dust and shows a wealth of star-forming regions, HII regions, and diffuse infrared cirrus (e.g. Fich & Terebey 1996). Extended Galactic infrared emission, long associated with the Galactic HI layer, is readily apparent as enhanced emission near the midplane (e.g. Terebey & Fich 1986, Sodroski et al. 1989). Each panel covers  $11.5^\circ$  in longitude. The dynamic range is much larger than can be displayed, therefore the stretch is logarithmic, with the range chosen separately for each panel to emphasize the most structure.

The complete set of available images and ancillary maps is illustrated for an individual  $1.4^\circ \times 1.4^\circ$  field near IC 1805 in the second Galactic quadrant. Figure 18 shows the coadded and resolution enhanced images plus beam sample maps. Figure 19 shows the associated diagnostic ancillary maps (see Sec. 2). The source IC 1805, an OB cluster exhibiting strong winds and ionizing radiation, is located near the brightest FIR emission. To the north, a cloud suffering erosion from the IC 1805 cluster appears in the infrared as a cometary shaped arc (Heyer et al. 1996). An HI survey of the region shows that the OB cluster appears to fuel a Galactic chimney (Normandeau, Taylor, & Dewdney 1996).

## 7. Summary

The *IRAS* Galaxy Atlas, an atlas of the Galactic plane ( $-4.7^\circ < b < 4.7^\circ$ ) plus the molecular clouds in Orion,  $\rho$  Ophiuchus, and Taurus-Auriga, has been produced at 60 and

100  $\mu\text{m}$  from *IRAS* data. The HIRES processor, which incorporates the MCM resolution enhancement algorithm, was ported to the Caltech parallel supercomputers for the CPU intensive task.

At 60  $\mu\text{m}$  the typical resolution is  $2.0' \times 4.7'$  for coadded IGA(1) (iteration = 1) images, and  $1.0' \times 1.7'$  for resolution enhanced IGA(20) images, which compares favorably with the  $50''$  diffraction limit of the *IRAS* telescope and the  $5'$  resolution of the previously released *IRAS* Sky Survey Atlas (ISSA). At 100  $\mu\text{m}$ , where the diffraction limit is  $84''$ , the typical IGA(1) resolution is  $3.8' \times 5.4'$  and IGA(20) resolution is  $1.7' \times 2.2'$ , again compared with the  $5'$  ISSA resolution.

The IGA contains images, beam sample maps to assess local resolution, and ancillary diagnostic maps in FITS format. Field sizes are  $1.4^\circ \times 1.4^\circ$  in the Galactic plane, and  $2.5^\circ \times 2.5^\circ$  in the Orion,  $\rho$  Ophiuchus, and Taurus-Auriga molecular clouds.

Zodiacal emission has been removed from the images. The result is images which are easily mosaicked by simple cropping and contain negligible seams. Stripes in the images, long the limiting artifact of standard HIRES processing, have been eliminated by algorithmic improvements to the destriping procedure. “Ringing” around point sources is the major artifact remaining in the IGA images.

Photometry on the IGA images is accurate to roughly 25%, depending on the wavelength and size scale, while positions agree with the *IRAS* Point Source Catalog to better than  $8''$  standard of deviation.

The IGA, combined with other Galactic plane surveys of similar ( $\sim 1'$ ) resolution, provides a powerful venue for multi-wavelength studies of the interstellar medium, star formation and large scale structure in our Galaxy.

We are indebted to Ron Beck and Diane Engler who carried out the production and recurring rounds of reprocessing of the IGA. We thank John Fowler for his help with the YORIC software. The project received support from the Astrophysics Data Program of the National Aeronautics and Space Administration under contract No. NAS5-32642. This work was performed in part at the Jet Propulsion Laboratory, California Institute of Technology, under a contract with the National Aeronautics and Space Administration. The atlas production was performed in part using the Intel Paragon operated by Caltech on behalf of the Concurrent Supercomputing Consortium.

## REFERENCES

- Assendorp, R. Bontekoe, T. J. R., Dejonge, A. R. W., Kester, D. J. .M., Roelfsema, P. R., & Wesselius, P R. 1995, A&AS, 110, 395
- Aumann, H. H., Fowler, J. W., & Melnyk, M. 1990, AJ, 99, 1674
- Beichman, C. A. 1987, ARAA, 25, 521
- Bontekoe, T. R., Koper, E. & Kester, D. J. M. 1994, A&A, 284, 1037
- Cao, Y. 1997. Parallel computing and the IRAS Galaxy Atlas, Ph.D. thesis, Caltech
- Cao, Y., Eggermont, P. P. B., & Terebey, S. 1997, submitted to IEEE Trans. Image Processing
- Cao, Y., Prince, T. A., Terebey, S., & Beichman, C. A., 1996, PASP, 108, 535
- Fich, M., & Terebey, S. 1996, ApJ, 472, 624
- Fowler, J. W. & Aumann, H. H., in Science with High Spatial Resolution Far-Infrared Data, Terebey, S. & Mazzarella, J. (eds.) 1994, (Pasadena: JPL 94-5)
- Frieden, B. R. & Wells, D. C. 1978, J. Opt. Soc. Am., 68, 93
- Good, J. C., in *IRAS Sky Survey Atlas Explanatory Supplement*, ed. Wheelock, S. L., Gautier, T. N. et al. 1994, App. G (Pasadena: JPL 94-11)
- Greisen, E. W. & Calabretta, M. 1996, submitted to A&A
- Heyer, M. H. 1996, in “CO: Twenty-Five Years of Millimeter Wave Spectroscopy”, Eds. W. Latter, D. Emerson, & S. Radford
- M.H. Heyer, M. H., Brund, C., Snell, R. L., Howe, J., Schloerb, F. P., Carpenter, J. C., Normandeau, M., Taylor, A. R., Cao, Y., Terebey, S., & Beichman, C. A. 1996, ApJ, 464, L175
- Hurt, R. L., & Barsony, M. 1996, ApJ, 460, L45
- IRAS* Catalogs and Atlases: Explanatory Supplement 1988, Beichman, C. A., Neugebauer, G., Habing, H. J., Clegg, P. E., & Chester, T. J. (editors) (Washington D.C.: GPO)
- IRAS* Point Source Catalog, Version 2 1988, Joint *IRAS* Science Working Group (Washington, D.C.: GPO)

- Kessler, M. F. 1995. The Infrared Space Observatory (*ISO*). *Space Sci. Rev.*, 74, 57
- Lucy, L. B., 1974, *AJ*, 79, 745
- Lucy, L. B. 1994, in “The Restoration of HST Images and Spectra – II”, pp. 79–85  
(Baltimore: STScI)
- Matsumoto, T. 1995. Infrared Telescope in Space – IRTS. *Space Sci. Rev.*, 74, 73
- Mill, J. D. & Guilmain, B. D. 1996. The *MSX* mission objectives. *Johns Hopkins Apl. Tech. Digest*, 17, 19
- Noriega-Crespo, A., Van Buren, D., Cao, Y. & Dgani, R. 1997, in preparation
- Normandeau, M., Taylor, A. P. & Dewdney, P. E. 1996, *Nature*, 380, 687
- Normandeau, M., Taylor, A. P. & Dewdney, P. E. 1997, *ApJS*, 108, 279
- Price, S. D. 1995. Infrared astronomy on the Midcourse Space Experiment. *Space Sci. Rev.*, 74, 81
- Rice, W., 1993, *AJ*, 105(1), 67
- Richardson, W. H., 1972, *J. Opt. Soc. Am.*, 62, 55
- Sodroski, T.J., Dwek, E., Hauser, M.G., & Kerr, F.J. 1989, *ApJ*, 336, 762
- Surace, J. A., Mazzarella, J. M., Soifer, B. T., & Wehrle, A. E. 1993, *AJ*, 105, 864
- Terebey, S., & Fich, M. 1986, *ApJ*, 309, L73
- Terebey, S. & Mazzarella, J. (eds.) 1994, *Science with High Spatial Resolution Far-Infrared Data*, (Pasadena: JPL 94-5)
- Wells, D. C., Greisen, E. W. & Harten 1981, R. H., *A&AS*, 44, 363
- Wheelock, S. L., Gautier, T. N. et al. 1994, *IRAS Sky Survey Atlas Explanatory Supplement*, (Pasadena: JPL 94-11)



Fig. 1.— Outline of the IGA Production Pipeline

Fig. 2.— Geometry of IGA fields in Galactic coordinates relative to the input Level 1 Plate data in equatorial coordinates. The Atlas covers  $-4.7^\circ < b < 4.7^\circ$ . The small shaded areas represent IGA fields ( $1.4^\circ \times 1.4^\circ$  on  $1^\circ$  centers), while the large shaded areas show Level 1 plates ( $7^\circ \times 7^\circ$  on  $5^\circ$  centers). The configuration shows an extreme case where  $1.4^\circ \times 1.4^\circ$  is the largest IGA field that can be fully covered by any single Level 1 plate.

Fig. 3.— Reprojection of Footprint Coordinates. In the diagram on the left, RA and Dec are known for the Level 1 plate center  $C$ , and  $x$  (negative as shown here) and  $y$  are known for the footprint  $P$ . The components of the unit vector  $OP$  is then computed (in equatorial system). As shown on the right, the vector  $OP$  is rotated to Galactic system, from which  $l$  and  $b$  of the footprint are obtained.

Fig. 4.— Dependence of Beam Size on Galactic Longitude. Left and right plots are for (a) 60 and (b) 100  $\mu\text{m}$  respectively. The top and bottom curves in each figure are the FWHM of the Gaussian fitted beam along the major and minor axes respectively. The regions in the Galactic plane which had intersecting scanlines in the *IRAS* survey are seen as two dips in the major axis curves (better resolution due to extra geometrical information).

Fig. 5.— Dependence of Beam Size on Source Flux. Resolution significantly improves for sources stronger than the local processing background of 33.7 Jy at 60  $\mu\text{m}$  and 223 Jy at 100  $\mu\text{m}$  in the test field. Results with destriping (solid lines), and non-destriping (dashed lines) show the IGA destriper has comparable resolution to standard HIRES, with the most notable difference along the 100  $\mu\text{m}$  major axis.

Fig. 6.— The ratio of (IGA(20) Flux / PSC Flux) vs. PSC Flux shows no trend with source strength. Offsets are discussed in text. Thirty-five sources are plotted in each wavelength band.

Fig. 7.— Illustrations of the Hysteresis Effect. (a). Internal flashes of known magnitude were used at the starting and ending points of a scanline, in an effort to determine the responsivity change (dashed line, assumed responsivity). The true responsivity is shown in the dashed curve, due to photon induced responsivity enhancement; (b). Computed fluxes from ascending and descending scans deviate from the true values; (c). The ratio of fluxes computed from ascending or descending scans varies with Galactic latitude. (Adapted with changes from Figure VI.B.2, *IRAS* Catalogs and Atlases: Expl. Suppl. 1988.)

Fig. 8.— Residual Hysteresis in the IGA. Left panels show the average intensity versus Galactic latitude at  $l = 0^\circ$ ,  $60^\circ$ , and  $120^\circ$ . Right panel shows the ratio of ISSA intensities from oppositely directed scans. The hysteresis signature (Fig. 7) is clearly seen near  $l = 0^\circ$ ,  $b = 0^\circ$  with an amplitude of about 20% at  $100 \mu\text{m}$  (upper right panel). Hysteresis may also be present in the  $l = 60^\circ$  and  $300^\circ$  graphs but is below the 5% level. Other small ( $< 5\%$ ) but systematic variations in the ISSA ratio are likely due to destriping differences.

Fig. 9.— Average Intensity and Ratio of ISSA Intensities from Opposite Scans,  $l = 180^\circ$ ,  $240^\circ$ , and  $300^\circ$ .

Fig. 10.— Minimum and Maximum Intensity Ratios vs. Galactic Longitude. Left:  $60 \mu\text{m}$ ; Right:  $100 \mu\text{m}$ . At  $100 \mu\text{m}$  and within  $60^\circ$  of the Galactic center, residual hysteresis becomes larger than systematic differences due to destriping and noise.

Fig. 11.— Demonstration of the Ringing Artifact. (a). 1st iteration,  $60 \mu\text{m}$ ; (b). 20th iteration,  $60 \mu\text{m}$ ; (c). 1st iteration,  $100 \mu\text{m}$ ; (d). 20th iteration,  $100 \mu\text{m}$ . Ringing is not seen for the 1st iteration images, but is prominent in the 20th. Field center is at  $l = 75^\circ$ ,  $b = 1^\circ$ ; field size is  $1.4^\circ$  on each side. Black is brighter in the images.

Fig. 12.— Demonstration of the Glitch Artifact. The elongated feature to the upper-left of the field center is a glitch. (a) and (b) show the glitch at 1st and 20th iteration respectively. At 20th iteration, the glitch takes a “broken-up” shape. Black is brighter in the images. Field center is  $l = 7^\circ$ ,  $b = 1^\circ$ , field size is  $1.4^\circ$  on each side.

Fig. 13.— Discontinuity Across One Subfield.  $60 \mu\text{m}$ , 20th iteration, field center is  $l = 48^\circ$ ,  $b = 1^\circ$ ,  $1.4^\circ$  on each side. The difference in intensity is approximately 5 MJy/sr. Black is brighter in the images.

Fig. 14.— *IRAS* Galaxy Atlas images of the Galactic plane at  $60\ \mu\text{m}$ . Longitudes  $0^\circ - 40^\circ$  show a variety of star-forming regions, HII regions, and the diffuse IR emission associated with the Galactic HI layer. Each panel covers  $11.5^\circ$  in longitude and  $-1.7^\circ < b < 1.7^\circ$  in latitude, with logarithmic stretch chosen to emphasize structure. Black is brighter in the images.

Fig. 15.— The Galactic Plane at  $60\ \mu\text{m}$ , Longitude  $40^\circ - 80^\circ$ .

Fig. 16.— The Galactic Plane at  $60\ \mu\text{m}$ , Longitude  $280^\circ - 320^\circ$ .

Fig. 17.— The Galactic Plane at  $60\ \mu\text{m}$ , Longitude  $320^\circ - 0^\circ$ .

Fig. 18.— Example  $1.4^\circ \times 1.4^\circ$  *IRAS* Galaxy Atlas images plus beam sample maps at  $60 \mu\text{m}$  near the IC1805 OB cluster. Black is brighter in the images. Top left shows the iteration = 1 image at the native *IRAS* resolution. There are several sources of diffuse emission and cirrus filaments in the field. The top right panel containing the iteration = 20 image illustrates how HIRES processing ‘sharpens’ features in the image. Many new discrete sources are now visible. Bottom panels: In the beam sample maps a field of artificial point sources helps to assess the effective spatial resolution in the IGA for faint *IRAS* sources. Bottom left panel exhibits the elliptical PSF which is typical in coadded *IRAS* images. Twenty iterations of HIRES processing (bottom right panel) pulls sources out of the background and sharpens the PSF but the point source ringing artifact appears (see Sec. 5.2). Notice that the PSF varies over the image. For strong sources, i.e. sources with high source-to-background contrast, the spatial resolution is better than indicated by the beam sample maps (see Sec. 4.1).

Fig. 19.— Examples of diagnostic ancillary maps for the field near the IC1805 OB cluster. The scanlines are evident in the detector track map (upper left) which shows the central positions of the *IRAS* detector samples projected into the image plane. The data coverage map (upper right) is the detector track map (upper left) convolved with the rectangular *IRAS* detector response profiles. This is the most useful diagnostic map for assessing HIRES image quality. Best HIRES results are obtained for high ( $>25$ ) and uniform coverage. The top border shows several regions of very low coverage (black) which can lead to artifacts (see Sec. 5.5). The photometric noise map (bottom left) provides a measure of the internal detector noise. A noisy detector scan will appear as a stripe. The correction factor variance map (bottom right) measures the fitting error in units of  $(S/N)^{-2}$ . High CFV values ( $> 0.1$ ) indicate noisy or unreliable parts of the image along the top and bottom borders (see Sec. 5.5).



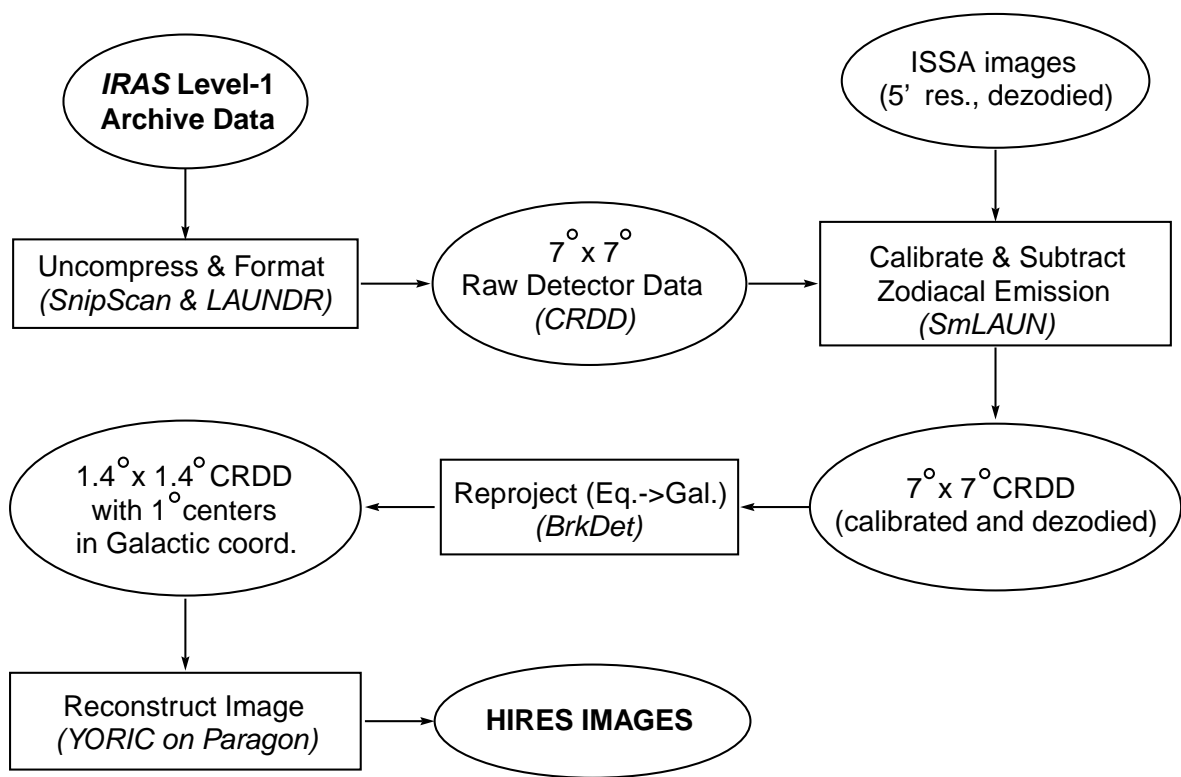


TABLE 1. Image and Ancillary Maps

Abbr. Name of Map	Name of Map	Quantity
IMG	image	$f_j$
PHN	photometric noise	$(\sum_i r_{ij}/\sigma_{ij}^2)^{-1/2}$ , where $\sigma_{ij} = \sigma_i[f_j/\sum_j(r_{ij}f_j)]$
CFV	correction factor variance	$[\sum_i(r_{ij}/\sigma_i^2)C_i^2]/[\sum_i(r_{ij}/\sigma_i^2)] - c_j^2$
CVG	coverage	$\sum_i r_{ij}$
DET	detector track	index of detector whose center falls at pixel $j$
BEM	beam sample map	reconstructed image from data made from spiked scene

This figure "figure2.jpg" is available in "jpg" format from:

<http://arxiv.org/ps/astro-ph/9705147v2>



TABLE 2. Comparison of PSC and IGA Fluxes

Source (IRAS PSC)	PSC Position	PSC Flux $60\mu\text{m}$ (Jy)	$100\mu\text{m}$	IGA Flux $60\mu\text{m}$ it=1	$100\mu\text{m}$ it=1	$60\mu\text{m}$ it=20	$100\mu\text{m}$ it=20
00270 + 6334	g120.5608 + 1.0782	59.91	97.30	76.248	119.645	79.770	132.628
00338 + 6312	g121.2980 + 0.6587	356.60	685.00	404.131	780.675	405.239	823.987
01243 + 6212	g127.1116 - 0.1152	31.30	72.97	36.112	64.307	36.292	73.700
07519 - 3404	g250.0056 - 3.3432	14.41	18.46	14.162	15.688	14.846	14.086
08011 - 3627	g253.0220 - 2.9951	26.12	11.96	27.792	17.614	29.650	16.778
08005 - 2356	g242.3643 + 3.5825	29.83	10.35	27.492	8.575	29.297	11.050
02071 + 6235	g131.8557 + 1.3320	32.90	57.23	40.276	64.815	45.801	75.912
02044 + 6031	g132.1572 - 0.7257	387.60	465.70	422.677	457.721	444.238	480.292
01304 + 6211	g127.8138 - 0.0226	194.00	50.18	190.435	47.181	197.142	51.815
02541 + 6208	g137.0688 + 3.0025	74.87	127.80	80.658	121.714	84.828	126.268
02175 + 5845	g134.2729 - 1.8974	32.44	61.79	38.913	66.829	39.420	85.632
02192 + 5821	g134.6198 - 2.1962	40.59	14.99	44.688	16.592	43.510	18.510
01420 + 6401	g128.7764 + 2.0125	128.80	234.40	164.751	231.846	171.442	251.556
01160 + 6529	g125.8047 + 3.0469	33.46	41.47	37.664	43.549	37.131	39.226
01145 + 6411	g125.7773 + 1.7256	57.71	80.60	72.848	94.677	74.204	95.384
20180 + 3558	g074.4973 - 0.1138	165.30	272.10	180.903	236.454	186.116	275.078
20306 + 3749	g077.4760 - 1.0817	187.00	316.30	194.880	272.214	183.857	319.383
20145 + 3645	g074.7535 + 0.9127	166.20	173.20	193.853	230.194	191.798	260.233
20116 + 3605	g073.8752 + 1.0260	242.20	267.00	247.650	234.989	242.372	347.049
20193 + 3448	g073.6944 - 0.9990	98.64	87.49	85.756	67.030	89.240	74.476
20144 + 3526	g073.6522 + 0.1946	432.60	364.10	503.915	355.433	417.726	268.931
20134 + 3444	g072.9526 - 0.0254	47.08	112.90	51.390	88.165	54.138	108.333
20142 + 3615	g074.2961 + 0.6794	42.29	83.16	53.566	75.882	42.222	67.248
20116 + 3605	g073.8752 + 1.0260	242.20	267.00	246.170	237.658	241.165	341.871
04365 + 4717	g157.6277 + 0.5289	32.51	55.33	34.552	63.570	36.884	67.212
07466 - 2631	g242.9404 - 0.4496	18.38	37.21	26.107	44.276	27.876	51.822
07466 - 2607	g242.5847 - 0.2401	13.28	28.25	12.806	23.050	13.404	31.760
07427 - 2400	g240.3153 + 0.0713	619.40	745.40	674.641	778.032	675.000	816.299
12437 - 6218	g302.3893 + 0.2788	408.40	679.60	475.944	686.172	457.197	711.096
12405 - 6219	g302.0211 + 0.2543	250.70	429.60	276.257	446.146	320.096	496.692
12377 - 6237	g301.7102 - 0.0561	123.90	196.80	141.933	163.958	158.350	204.141
12413 - 6332	g302.1507 - 0.9487	240.70	259.80	259.115	269.452	277.910	302.102
05378 + 2928	g178.9940 - 0.5414	9.46	22.36	10.740	23.204	10.744	23.257
16251 - 4929	g334.7223 - 0.6527	520.00	710.80	661.577	675.769	642.504	587.205
12268 - 6156	g300.4020 + 0.5459	193.00	269.60	237.519	317.504	248.148	349.192
12091 - 6129	g298.2623 + 0.7401	628.30	796.40	670.887	858.152	661.079	864.247

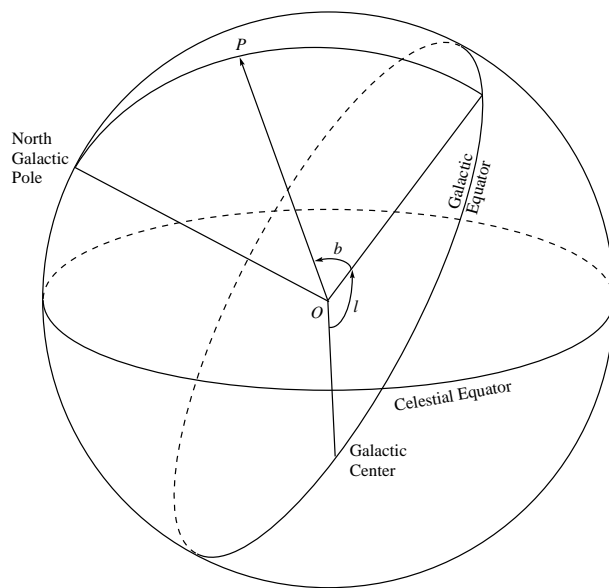
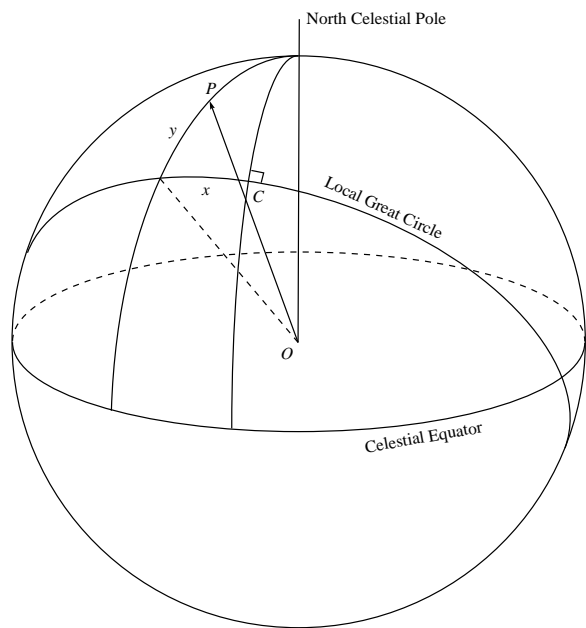
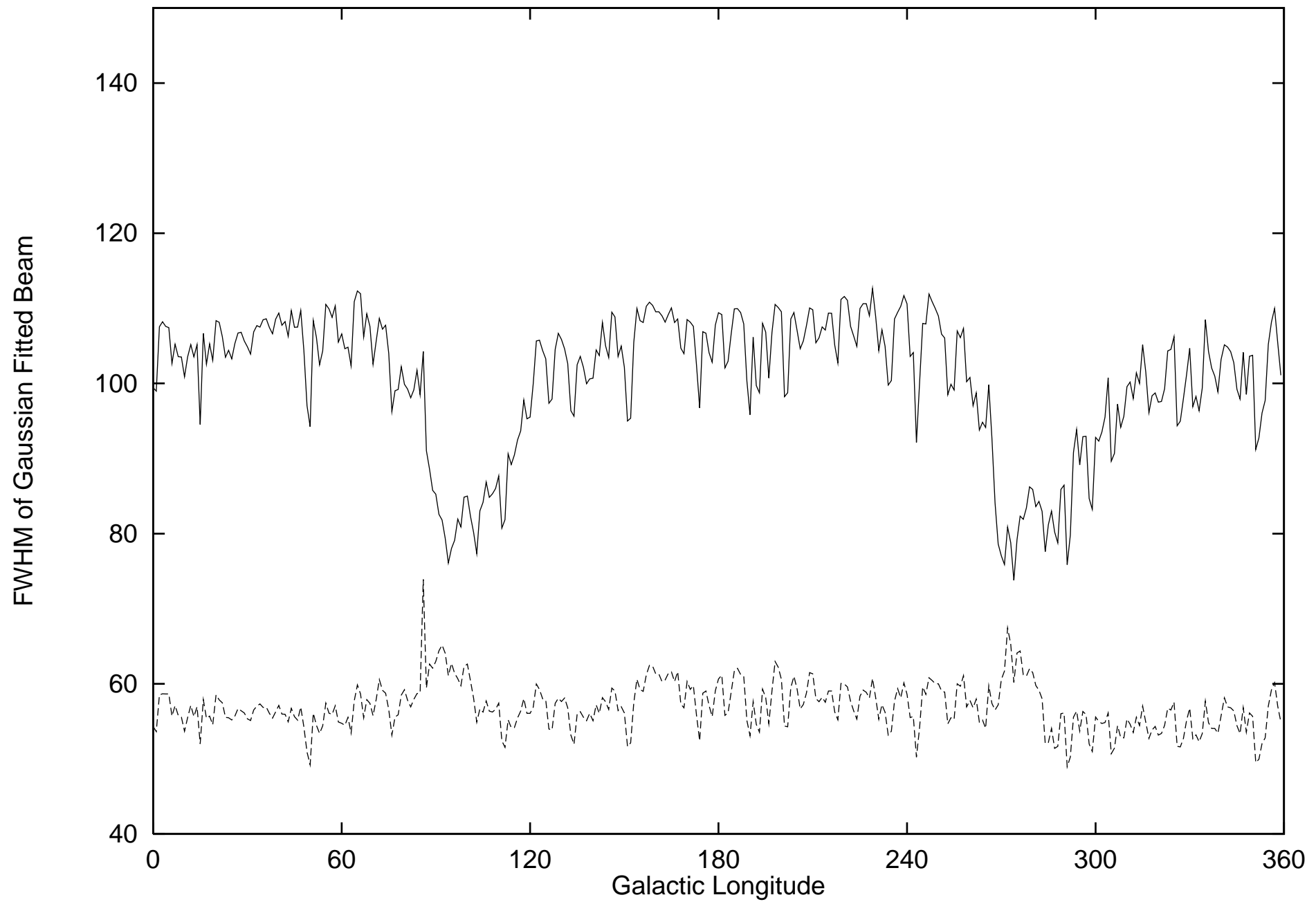


TABLE 3. Photometry Comparison Statistics

Band ( $\mu\text{m}$ )	Quantity	Mean	Std. Dev.
60	IGA(1)/PSC	1.12	0.11
60	IGA(20)/PSC	1.14	0.13
60	IGA(20)/IGA(1)	1.02	0.07
100	IGA(1)/PSC	1.01	0.16
100	IGA(20)/PSC	1.11	0.19
100	IGA(20)/IGA(1)	1.10	0.15

60 micron



100 micron

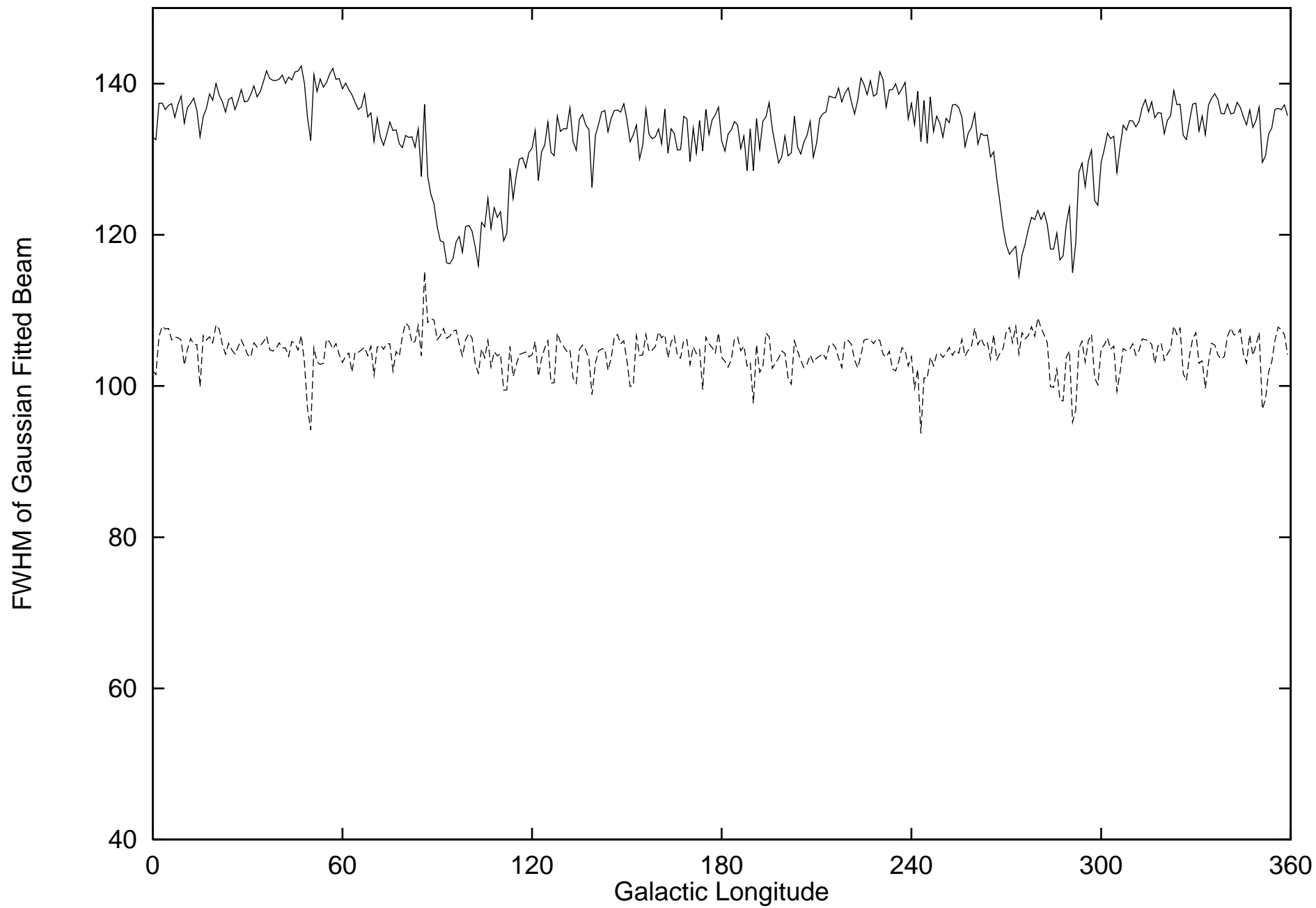
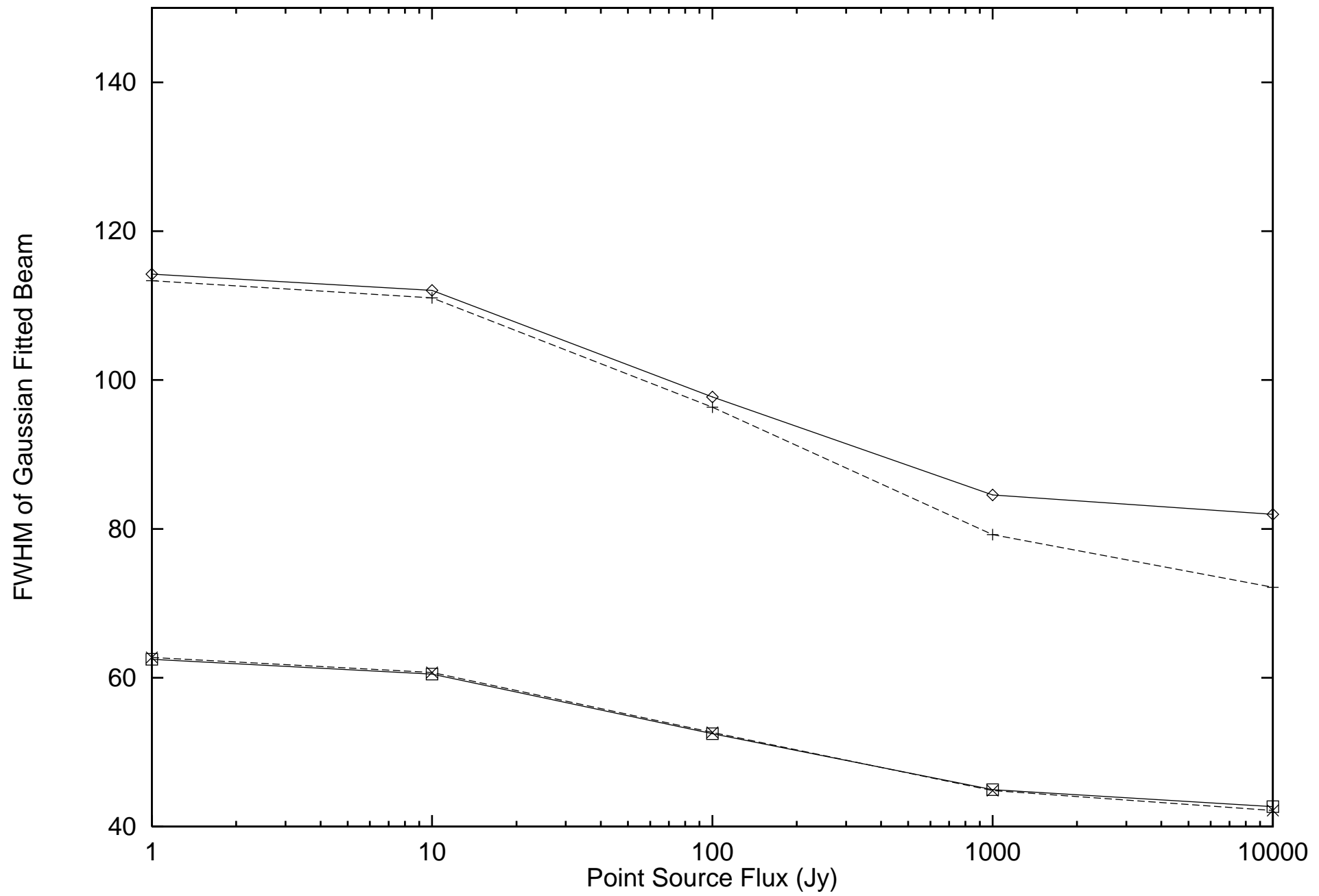


TABLE 4. Comparison of PSC and IGA Positions

Source (IRAS PSC)	PSC $l$	PSC $b$	IGA $60\mu\text{m } l$	IGA $60\mu\text{m } b$	IGA $100\mu\text{m } l$	IGA $100\mu\text{m } b$	Dist. $60\mu\text{m } (")$	Dist. $100\mu\text{m } (")$
00270 + 6334	120.5608	1.0782	120.5622	1.0797	120.5628	1.0804	7.4	10.7
00338 + 6312	121.2980	0.6587	121.2974	0.6561	121.2990	0.6590	9.6	3.8
01243 + 6212	127.1116	-0.1152	127.1108	-0.1155	127.1110	-0.1163	3.1	4.5
07519 - 3404	250.0056	-3.3432	250.0030	-3.3412	250.0032	-3.3421	11.8	9.5
08011 - 3627	253.0220	-2.9951	253.0210	-2.9960	253.0216	-2.9951	4.8	1.4
08005 - 2356	242.3643	3.5825	242.3653	3.5846	242.3619	3.5831	8.4	8.9
02071 + 6235	131.8557	1.3320	131.8539	1.3314	131.8544	1.3325	6.8	5.0
02044 + 6031	132.1572	-0.7257	132.1584	-0.7257	132.1581	-0.7243	4.3	6.0
01304 + 6211	127.8138	-0.0226	127.8140	-0.0210	127.8123	-0.0202	5.8	10.2
02541 + 6208	137.0688	3.0025	137.0696	3.0039	137.0695	3.0037	5.8	5.0
02175 + 5845	134.2729	-1.8974	134.2700	-1.8954	134.2703	-1.8938	12.7	16.0
02192 + 5821	134.6198	-2.1962	134.6205	-2.1954	134.6206	-2.1963	3.8	2.9
01420 + 6401	128.7764	2.0125	128.7749	2.0115	128.7740	2.0118	6.5	9.0
01160 + 6529	125.8047	3.0469	125.8044	3.0469	125.8053	3.0462	1.1	3.3
01145 + 6411	125.7773	1.7256	125.7733	1.7210	125.7764	1.7234	21.9	8.6
20180 + 3558	74.4973	-0.1138	74.4978	-0.1129	74.4970	-0.1125	3.7	4.8
20306 + 3749	077.4760	-1.0817	77.4765	-1.0828	77.4758	-1.0829	4.3	4.4
20145 + 3645	074.7535	0.9127	74.7529	0.9116	74.7531	0.9111	4.5	5.9
20116 + 3605	073.8752	1.0260	73.8739	1.0237	73.8741	1.0239	9.5	8.5
20193 + 3448	073.6944	-0.9990	73.6956	-0.9984	73.6943	-0.9988	4.8	0.8
20144 + 3526	073.6522	0.1946	73.6542	0.1962	73.6547	0.1971	9.2	12.7
20134 + 3444	072.9526	-0.0254	72.9543	-0.0244	72.9542	-0.0245	7.1	6.6
20142 + 3615	074.2961	0.6794	74.2965	0.6776	74.2963	0.6784	6.6	3.7
20116 + 3605	073.8752	1.0260	73.8738	1.0238	073.8740	1.0239	9.4	8.7
04365 + 4717	157.6277	0.5289	157.6315	0.5351	157.6299	0.5323	26.2	14.6
07466 - 2631	242.9404	-0.4496	242.9418	-0.4529	242.9410	-0.4526	12.9	11.0
07466 - 2607	242.5847	-0.2401	242.5900	-0.2424	242.5891	-0.2428	20.8	18.6
07427 - 2400	240.3153	0.0713	240.3157	0.0707	240.3153	0.0709	2.6	1.4
12437 - 6218	302.3893	0.2788	302.3894	0.2779	302.3888	0.2764	3.2	8.8
12405 - 6219	302.0211	0.2543	302.0208	0.2546	302.0208	0.2542	1.5	1.1
12377 - 6237	301.7102	-0.0561	301.7098	-0.0550	301.7096	-0.0550	4.2	4.5
12413 - 6332	302.1507	-0.9487	302.1501	-0.9483	302.1485	-0.9485	2.6	8.0
05378 + 2928	178.9940	-0.5414	178.9968	-0.5401	178.9960	-0.5414	11.1	7.2
16251 - 4929	334.7223	-0.6527	334.7210	-0.6520	334.7213	-0.6518	5.3	4.8
12268 - 6156	300.4020	0.5459	300.4012	0.5441	300.4003	0.5446	7.1	7.7
12091 - 6129	298.2623	0.7401	298.2631	0.7411	298.2616	0.7415	4.6	5.6

60 micron



100 micron

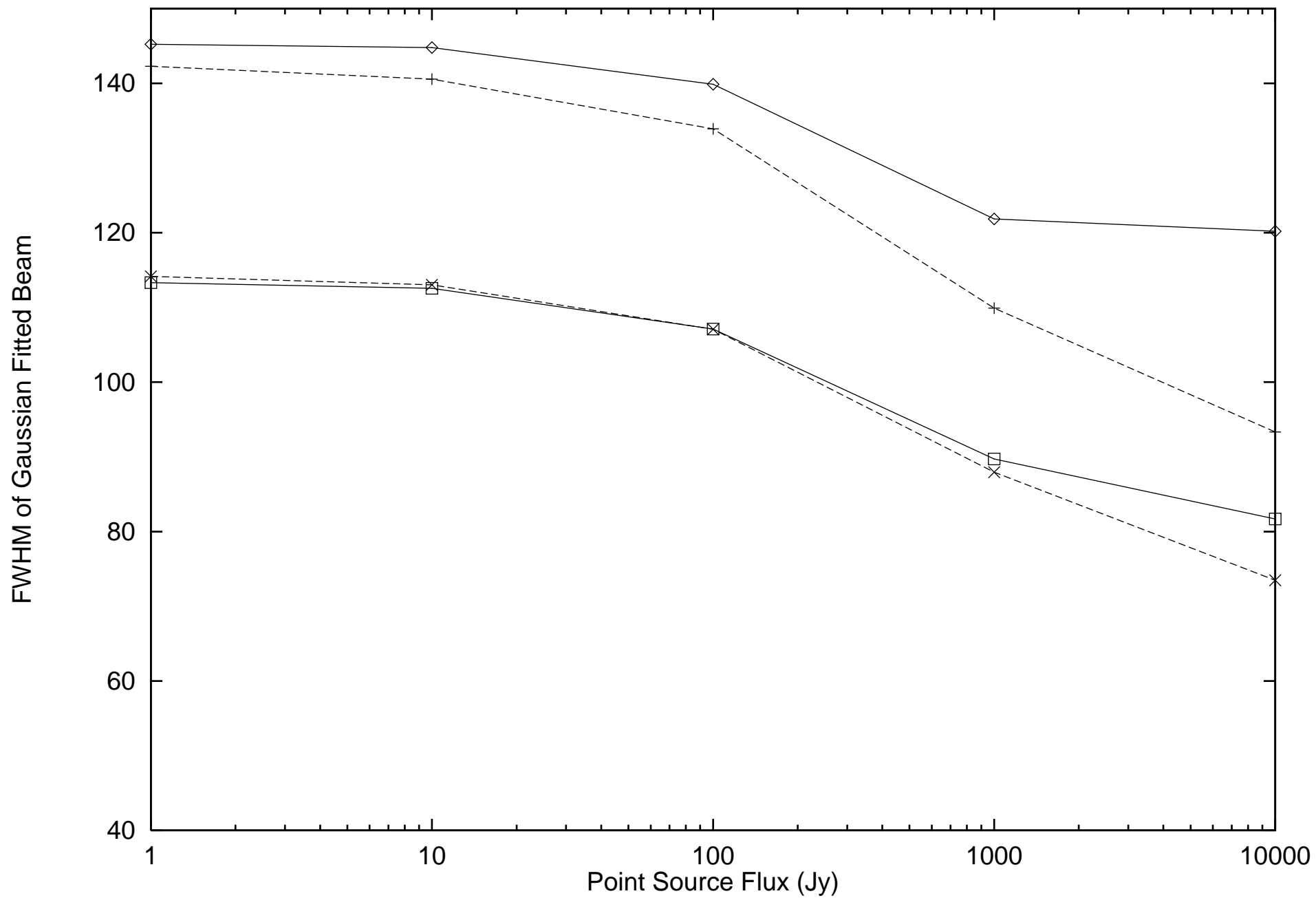
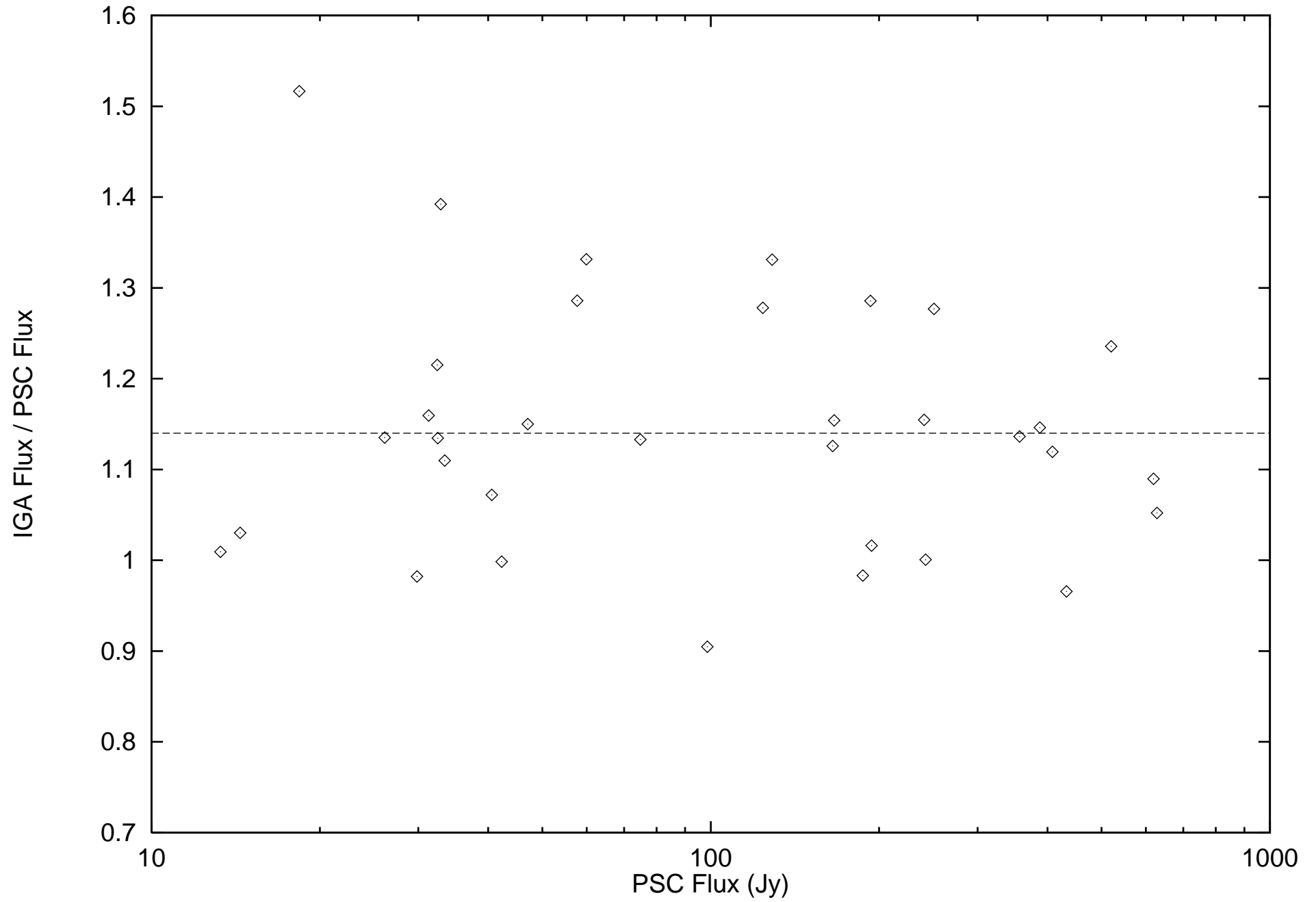




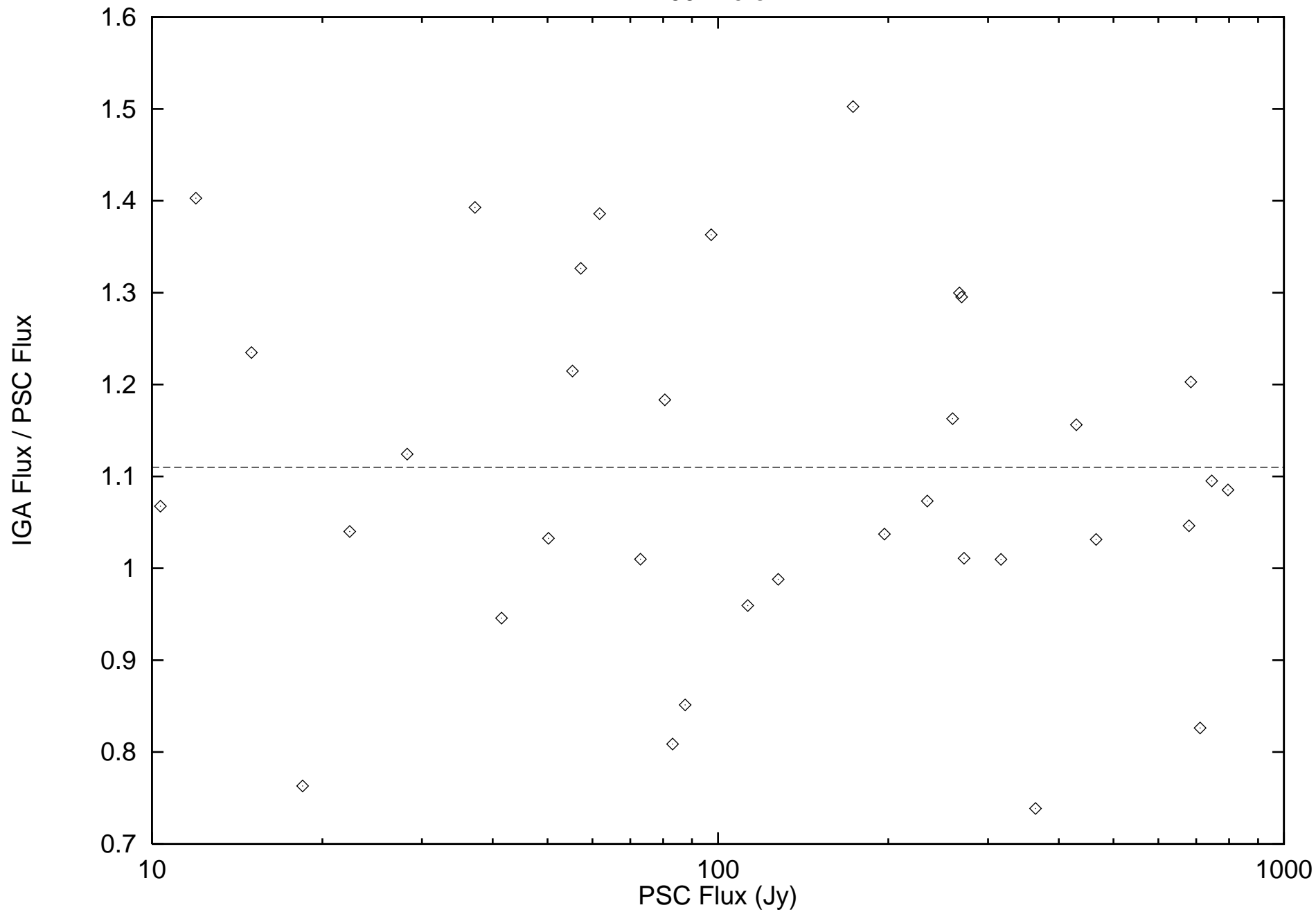
TABLE 5. Statistics of Pixel Intensity Ratios for Neighboring Subfields

Iteration	Wavelength	Cross Level 1 Plate?	Number of Pixels	Standard Deviation of Ratio
1	60 $\mu\text{m}$	no	10122	0.14%
1	60 $\mu\text{m}$	yes	8194	0.52%
1	100 $\mu\text{m}$	no	10122	0.08%
1	100 $\mu\text{m}$	yes	8194	0.18%
20	60 $\mu\text{m}$	no	10122	0.51%
20	60 $\mu\text{m}$	yes	8194	1.5%
20	100 $\mu\text{m}$	no	10122	0.23%
20	100 $\mu\text{m}$	yes	8194	0.46%

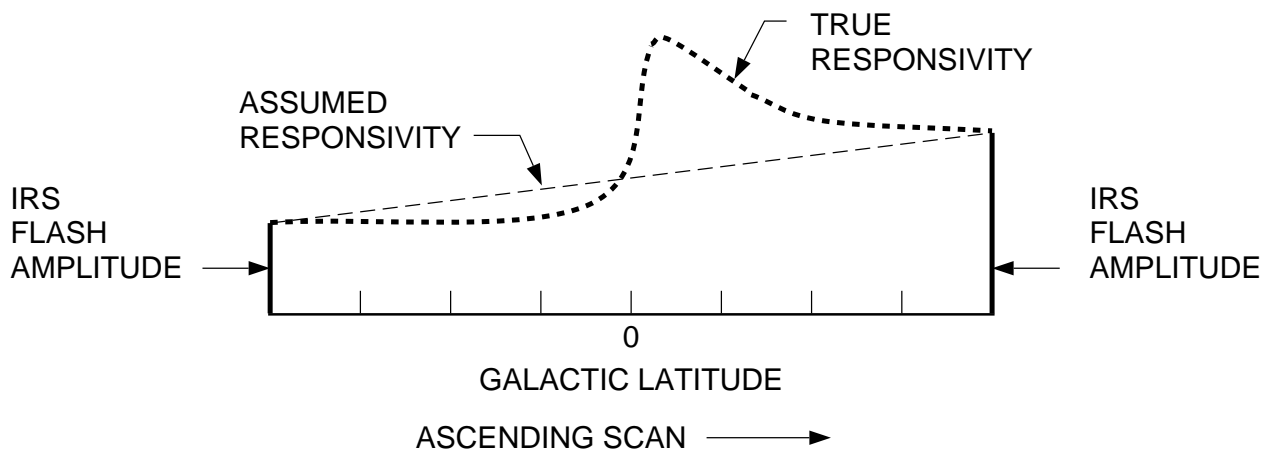
60 micron



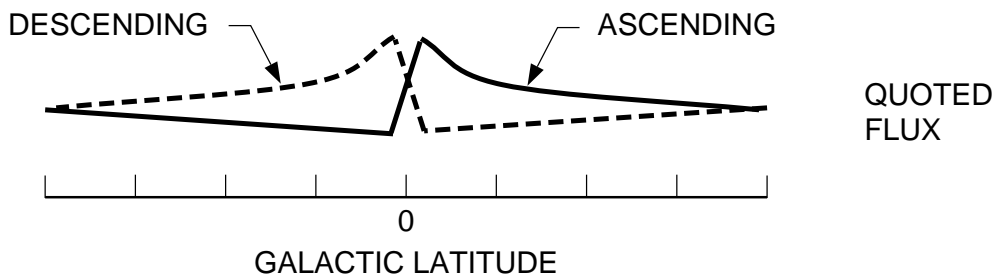
100 micron



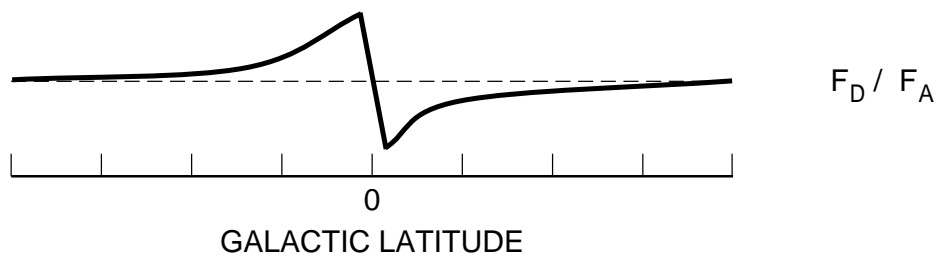
(a)

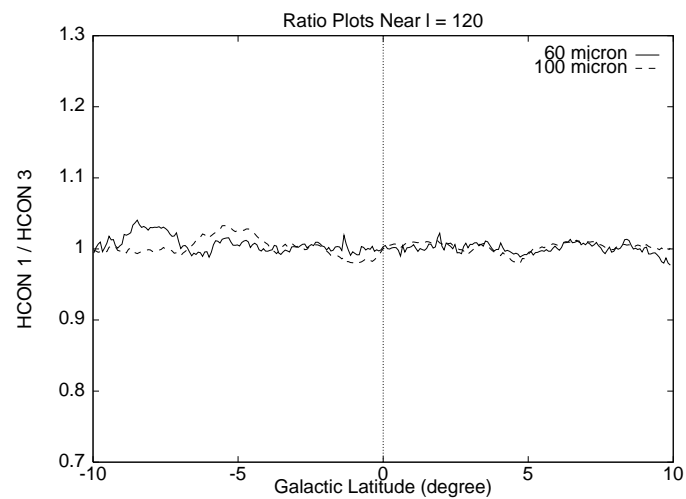
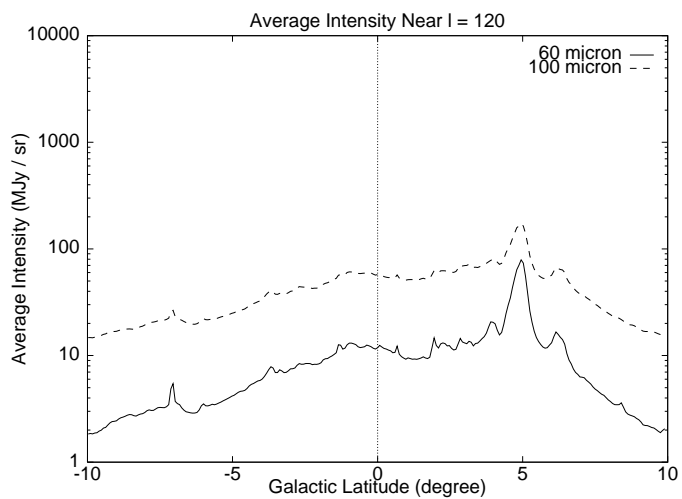
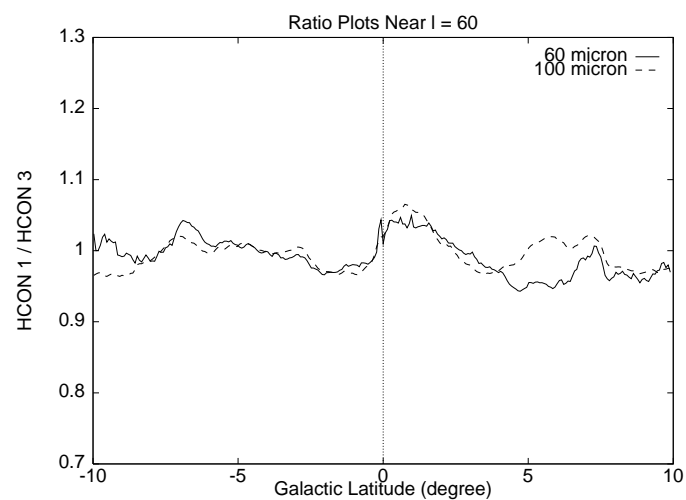
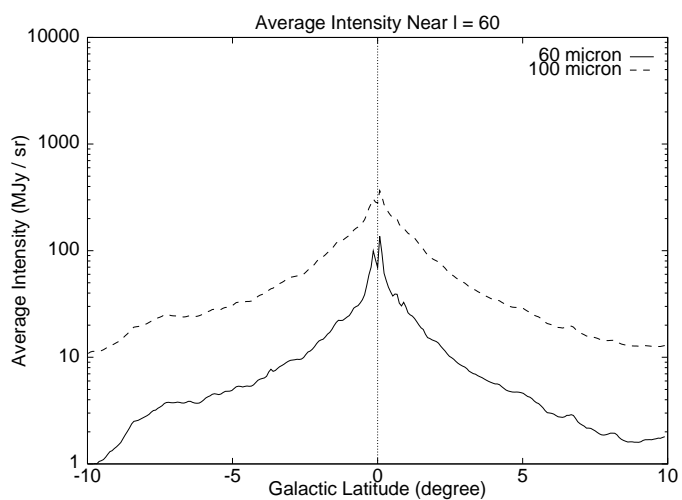
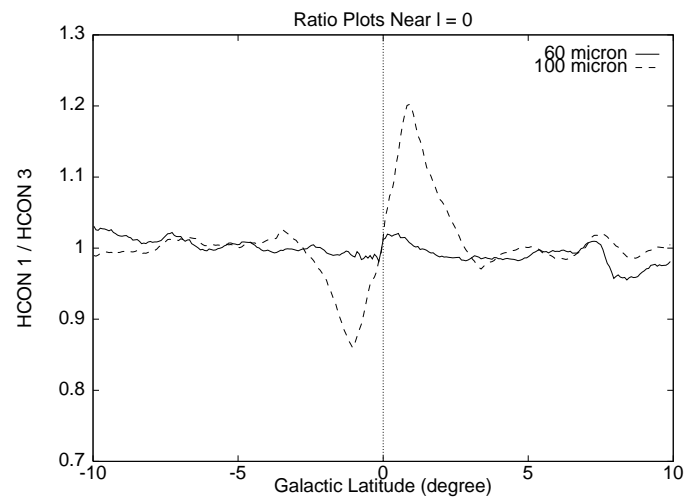
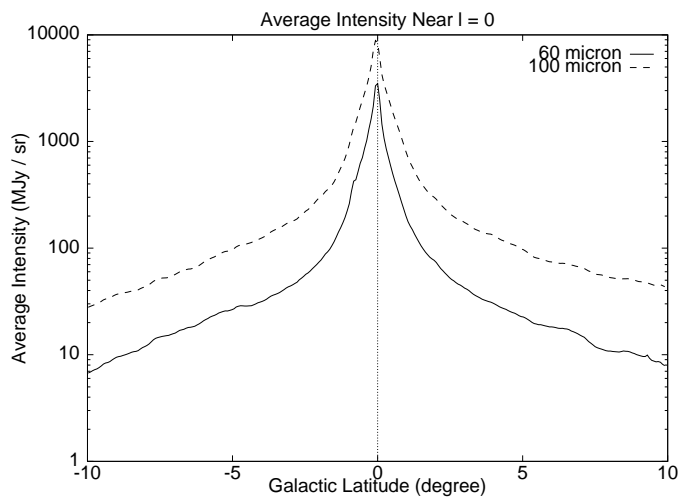


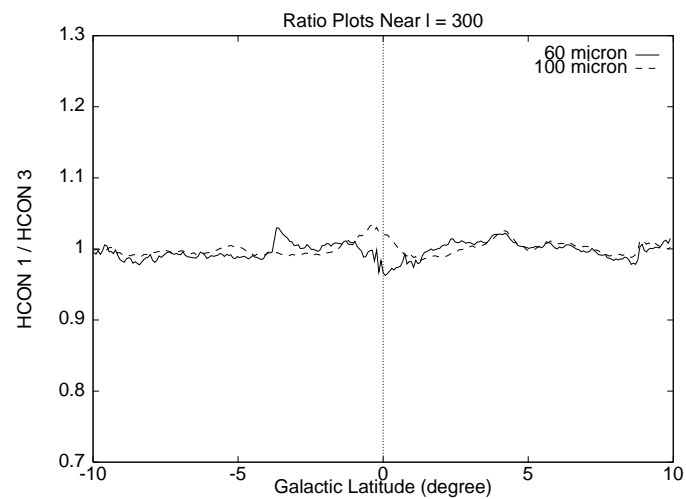
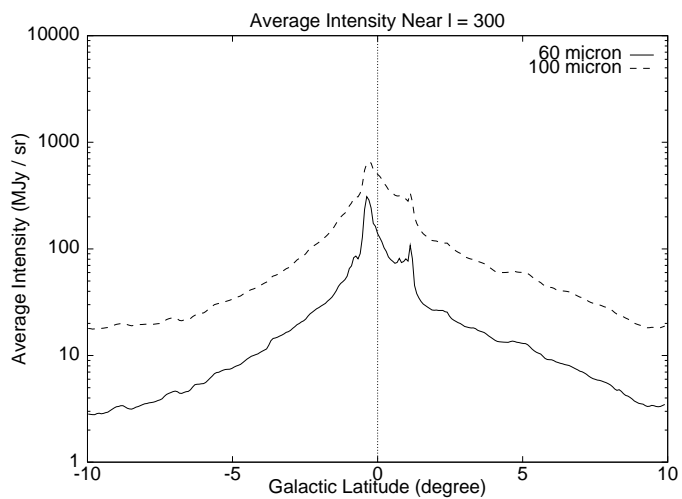
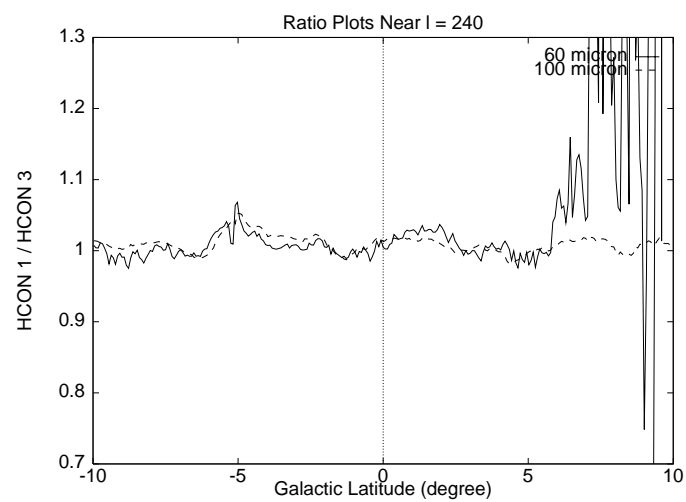
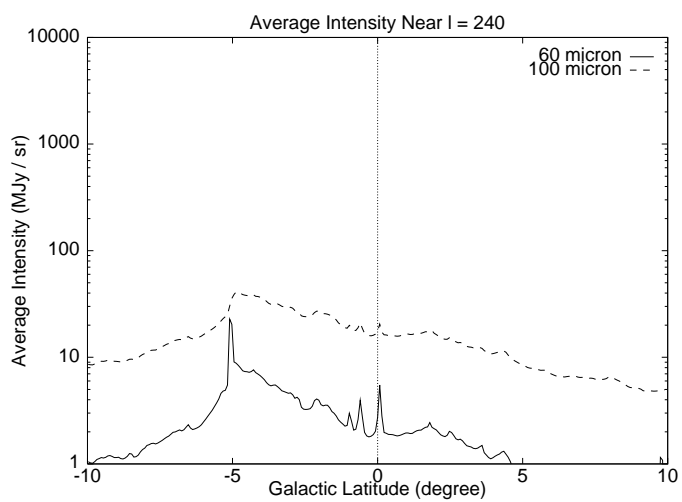
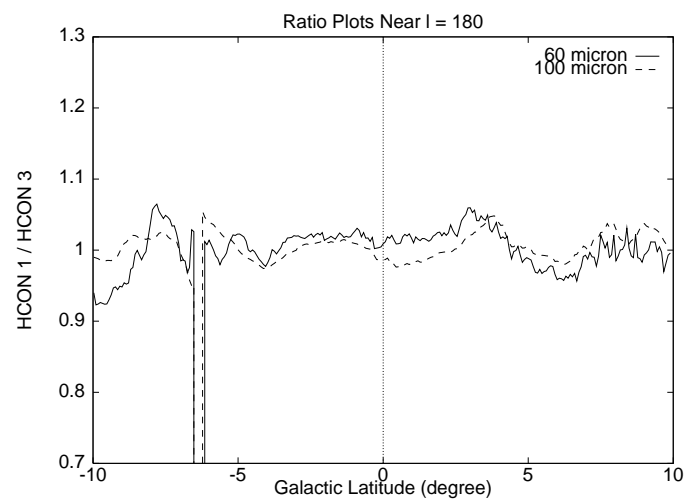
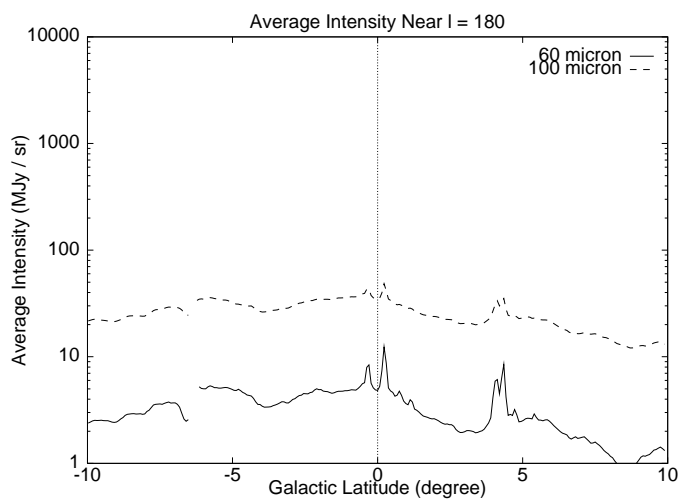
(b)



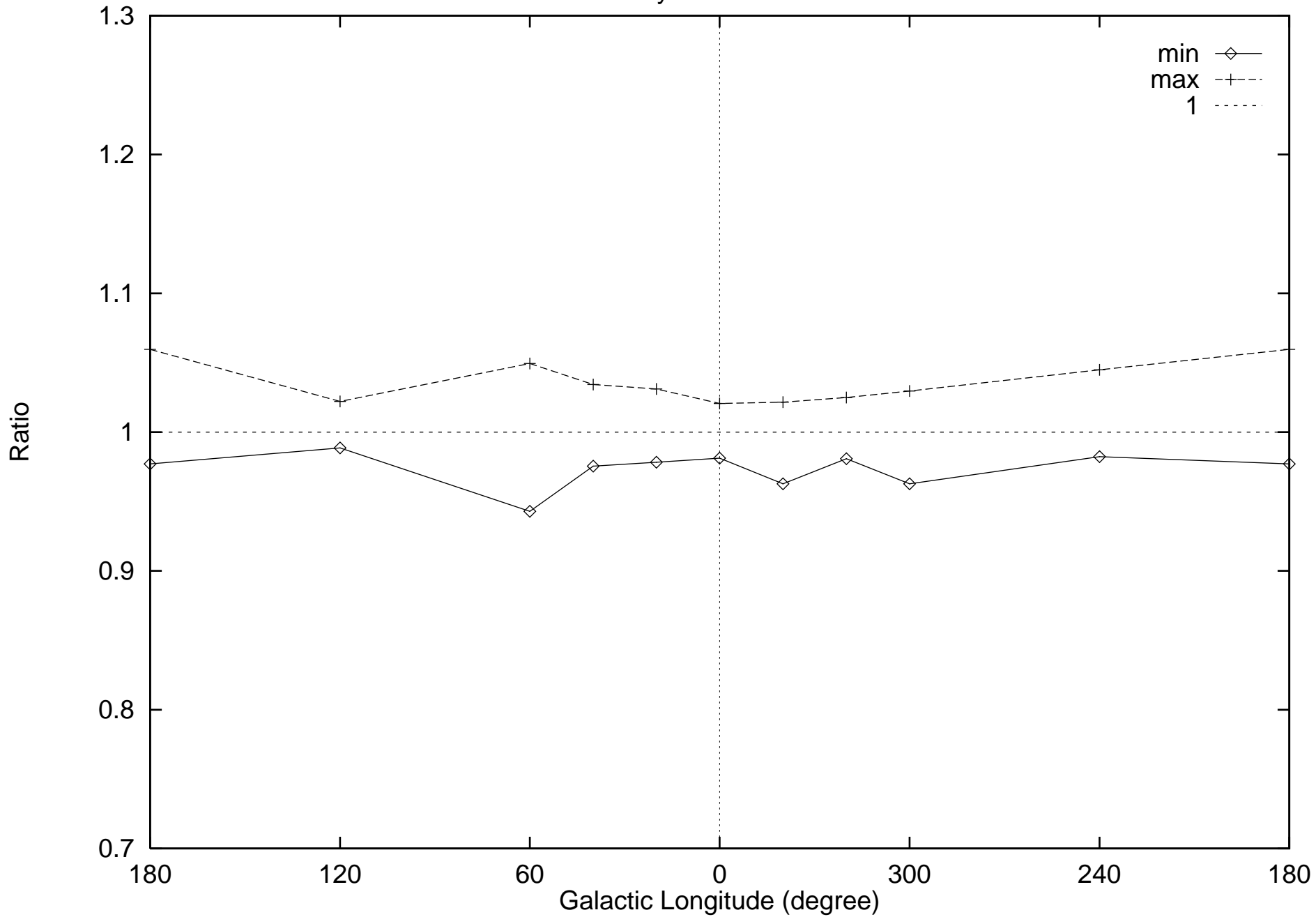
(c)



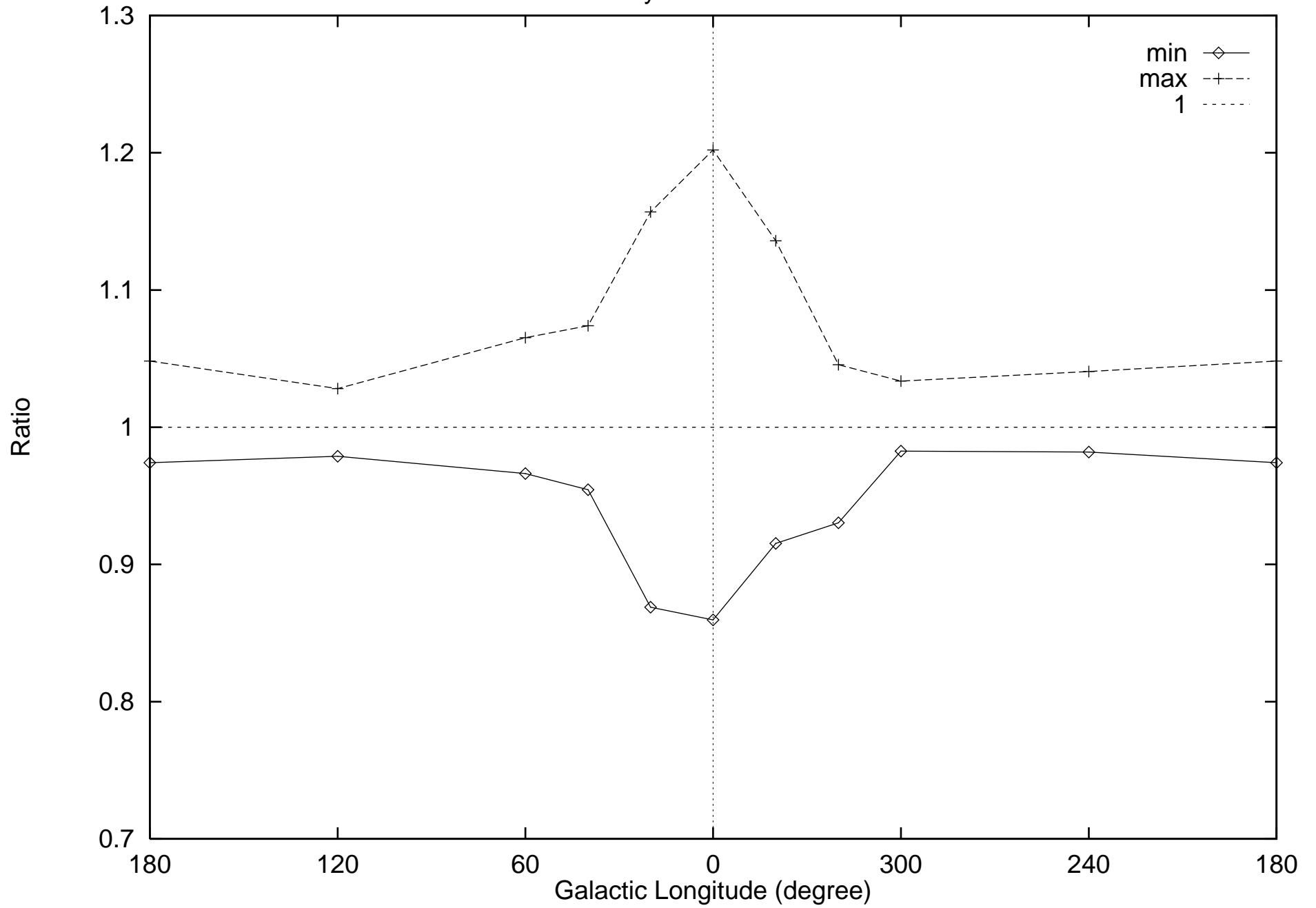




Residual Hysteresis at 60 Micron



Residual Hysteresis at 100 Micron





This figure "figure11.jpg" is available in "jpg" format from:

<http://arxiv.org/ps/astro-ph/9705147v2>

This figure "figure12.jpg" is available in "jpg" format from:

<http://arxiv.org/ps/astro-ph/9705147v2>

This figure "figure13.jpg" is available in "jpg" format from:

<http://arxiv.org/ps/astro-ph/9705147v2>

This figure "figure14.jpg" is available in "jpg" format from:

<http://arxiv.org/ps/astro-ph/9705147v2>

This figure "figure15.jpg" is available in "jpg" format from:

<http://arxiv.org/ps/astro-ph/9705147v2>

This figure "figure16.jpg" is available in "jpg" format from:

<http://arxiv.org/ps/astro-ph/9705147v2>

This figure "figure17.jpg" is available in "jpg" format from:

<http://arxiv.org/ps/astro-ph/9705147v2>

This figure "figure18.jpg" is available in "jpg" format from:

<http://arxiv.org/ps/astro-ph/9705147v2>



This figure "figure19.jpg" is available in "jpg" format from:

<http://arxiv.org/ps/astro-ph/9705147v2>